https://doi.org/10.5194/egusphere-2026-345
Preprint. Discussion started: 4 March 2026

A 2020 permafrost distribution map over the Qinghai-Tibet Plateau

Yuhong Chen[1], Zhuotong Nan[2,3], Wenbiao Tian[3], Yi Zhao[4], Shuping Zhao[3], Dongkai Yang[1], Guifei Jing[1], and Fujun Niu[2]

[1] Hangzhou International Innovation Institute, Beihang University, Hangzhou, China
[2]Yangtze River Delta Urban Wetland Ecosystem National Field Scientific Observation and Research Station, School of Environment and Geographic Sciences, Shanghai Normal University, Shanghai, 200234, China
[3]State Key Laboratory of Climate System Prediction and Risk Management, Nanjing Normal University, Nanjing, 210023, China
[4] Key Laboratory of Water and Sediment Sciences, Ministry of Education, College of Environmental Sciences and Engineering, Peking University, Beijing, China

Correspondence to: Zhuotong Nan (nanzt@njnu.edu.cn)

Abstract. Permafrost on the Qinghai-Tibet Plateau (QTP) is undergoing rapid degradation, yet most existing distribution maps reflect long-term historical averages, failing to capture the current thermal state required for accurate ecological and hydrological modeling. To address this temporal mismatch, this study presents a 1-km QTP permafrost distribution map for the year 2020. We employed an extended ground surface frost number model (FROSTNUM) driven by satellite-derived freezing/thawing indices. To overcome the lack of concurrent field surveys for parameter calibration, we implemented a space-for-time substitution strategy, utilizing a Random Forest regression to robustly estimate the empirical soil parameter (E) based on environmental covariates. The resulting map reveals that in 2020, permafrost covered approximately 1.038×10^6 km² (39.35% of the plateau), while seasonally frozen ground (SFG) covered 1.466×10^6 km² (55.57%). Compared to the 2010 baseline, the permafrost area declined by 4.8×10^4 km² (a 1.82% decrease). Spatially, the degradation of permafrost to SFG extensively occurred in the central QTP (accounting for 7.41% of the total change), and a significant marginal contraction of SFG to non-frozen ground in the southern margin (accounting for 39.62% of the total change). Validations against 109 independent borehole records from the 2020 period confirms the map's reliability, achieving an overall accuracy of 0.84 and a Kappa of 0.58. This 2020 map provides an essential, up-to-date resource for quantifying the recent cryospheric shifts and supporting engineering risk assessments in this climate-sensitive region.

1 Introduction

Permafrost, defined as ground that remains below 0 °C for at least two consecutive years (Lewkowicz et al., 2025), underlies approximately 24% of the exposed land surface in the Northern Hemisphere (Obu et al., 2019; Zhang et al., 1999). As a critical component of the cryosphere, permafrost is highly sensitive to climate fluctuations and human interference (Burke et al., 2020; Chadburn et al., 2017; Smith et al., 2022). The Qinghai-Tibet Plateau (QTP), known as the "Third Pole" and "Asian Water Tower", hosts the largest extent of permafrost in the mid- and low-latitude regions (Zhao et al., 2004). Due to its unique high-altitude environment, QTP permafrost is characterized by relatively high temperatures and low thermal stability, making it particularly responsive to warming trends (Li et al., 2008; Yang et al., 2019; Yao et al., 2022). Under ongoing global

https://doi.org/10.5194/egusphere-2026-345
Preprint. Discussion started: 4 March 2026

warming, permafrost degradation on the plateau has triggered profound impacts on regional hydrological processes (Tananaev and Lotsari, 2022), carbon cycling (Mu et al., 2020), ecosystem stability (Yang et al., 2010), and the safety of critical engineering infrastructure (Hjort et al., 2022). These widespread impacts underscore the critical importance of producing high-quality, up-to-date permafrost maps, which serve as indispensable foundational datasets for quantifying environmental changes and supporting risk assessments in cold regions (Kim et al., 2024; Obu et al., 2019).

Although numerous permafrost maps of the QTP have been compiled (Guo and Wang, 2013; Zou et al., 2017), the evolution of mapping strategies reflects a continuous struggle against data scarcity. Early maps were manually delineated on topographic bases using expert judgement and limited data sources, such as air temperature and field surveys (Cheng et al., 1996; Mi, 1990). While pioneering, these methods were prone to subjectivity. Subsequent studies adopted empirical or semi-physical models for mapping, including altitude model (Li and Cheng, 1999), mean annual ground temperature (MAGT) model (Nan et al., 2002; Ran et al., 2022), frost number model (Nan et al., 2013; Shan et al., 2022), and the temperature at the top of permafrost (TTOP) model (Obu et al., 2019; Zou et al., 2017). To overcome the sparsity of in-situ observations, latest semi-physical model studies extensively used remote sensing and reanalysis datasets (Hachem et al., 2009; Zou et al., 2017). While these extensive datasets mitigate the spatial gaps of ground station networks, they introduce inherent uncertainties. Remote sensing products, particularly land surface temperature (LST), are frequently plagued by cloud contamination, leading to significant data gaps (Yu et al., 2015). Conversely, reanalysis datasets, while spatially complete, often suffer from coarse spatial resolution and considerable uncertainty in complex terrain (Hu et al., 2019; Mao et al., 2010). More recently, physically-based land surface models (LSMs) (e.g. (Zhang et al., 2019; Zhao et al., 2022)) and machine learning approaches (e.g. (Ni et al., 2021; Zhang et al., 2024)) have been employed to capture complex process mechanisms and non-linear relationships. While LSMs can theoretically simulate temporal evolution, they are prone to considerable uncertainty when upscaled to the heterogeneous QTP without extensive calibration, and pure machine learning models often suffer from spatial biases due to the lack of representative training data across the vast plateau (Gay et al., 2023; Siewert, 2018).

Beyond these data source limitations, a fundamental temporal deficiency persists across most existing products: they largely reflect long-term historical average conditions rather than the current distribution of frozen ground. Because ground observations on the QTP are sparse and unevenly distributed, mostly concentrated along transportation corridors, previous mapping efforts often aggregated data across multiple decades to maximize sample size. Consequently, these maps depict a composite state that smooths over the rapid climatic shifts of past decades. This reliance on climatological averages creates a temporal mismatch, hindering the accurate validation of land surface models and ecological assessments that require precise, year-specific benchmarks.

To address the need for a temporally specific benchmark, our previous work (Cao et al., 2023) developed a high-quality permafrost distribution map for the specific year of 2010. That study employed an extended ground surface frost number model (FROSTNUM), incorporating cloud-gap-filled satellite freezing/thawing indices and an empirical soil parameter (E) calibrated against extensive survey data from the 2009–2010 period. It successfully provided the first instantaneous snapshot of the QTP

https://doi.org/10.5194/egusphere-2026-345
Preprint. Discussion started: 4 March 2026

permafrost distribution and has been widely used since its publication (e.g. (Deng et al., 2024; Pan et al., 2024; Zhong et al., 2024)).

Nevertheless, the climate on the QTP has changed rapidly during the 2010–2020 decade (Hu et al., 2024; Zhao et al., 2025), making the 2010 map increasingly outdated for contemporary applications. Producing a comparable map for 2020 is challenging because the extensive field surveys available for 2010 were not repeated in 2020. To fill this gap, this study presents a new, high-accuracy 1-km QTP permafrost map for 2020. We refine the FROSTNUM mapping framework (Cao et al., 2023; Hu et al., 2020) by introducing a space-for-time substitution strategy. We hypothesize that while climatic drivers (freezing and thawing indices) have shifted, the fundamental relationship between the empirical soil parameter (E) and environmental covariates (e.g., topography, soil texture, soil moisture) has remained applicable. By evaluating transfer learning strategies, comparing neural network and Random Forest (RF) approaches, we derive the 2020 E parameter from 2010 relationships. The resulting map provides a critical, up-to-date dataset for quantifying decadal permafrost changes and supporting future high-precision modeling on the QTP.

2 Study area and data

2.1 Study area

The QTP, widely referred to as the "Third Pole" and the "Asian Water Tower," is the highest and most extensive plateau in the world. Bounded within 26-40 °N and 73.5-104.5 °E, it spans an area of approximately 2.5×10^6 km^2 with an average elevation exceeding 4000 m above sea level (a.s.l.) (Fig. 1). As the headwaters of major Asian river systems, including the Yangtze, Yellow River, Indus, Mekong, and Ganges, the plateau plays a critical role in the regional hydrological cycle and supports water resources for downstream populations.

The plateau is characterized by a distinctive high-altitude cryospheric environment, with extensive distribution of glaciers, snow cover, and permafrost (Qiu, 2008; Yao et al., 2012).The climate is governed by the interplay between the westerlies and the Asian monsoon, creating a pronounced climatic gradient. Mean annual air temperature generally ranges from -5°C and 5 °C (Zhang et al., 2019), while mean annual precipitation decreases from over 700 mm in the humid southeast to less than 50 mm in the arid northwest (Peng et al., 2019). Approximately 70% of annual precipitation occurs during the monsoon season from May to September (Kukulies et al., 2020; Zhu et al., 2020).

Vegetation cover transitions from alpine forests and meadows in the southeast to alpine steppes and deserts in the northwest (Zhou et al., 2025). Correspondingly, permafrost thickness varies significantly, ranging from a few meters in marginal zones to approximately 350 m in the interior, with the depth of zero annual amplitude typically varying between 3.5 to 17 m (Zhao et al., 2020).

Crucially, the QTP is experiencing rapid climate warming. Between 1960 and 2015, the annual mean temperature increased at a rate of 0.33 °C/10a, more than double the global warming rate (0.14 °C/10a) (Zhang et al., 2020). This accelerated warming has intensified cryospheric instability, necessitating up-to-date monitoring of permafrost distribution.

https://doi.org/10.5194/egusphere-2026-345
Preprint. Discussion started: 4 March 2026

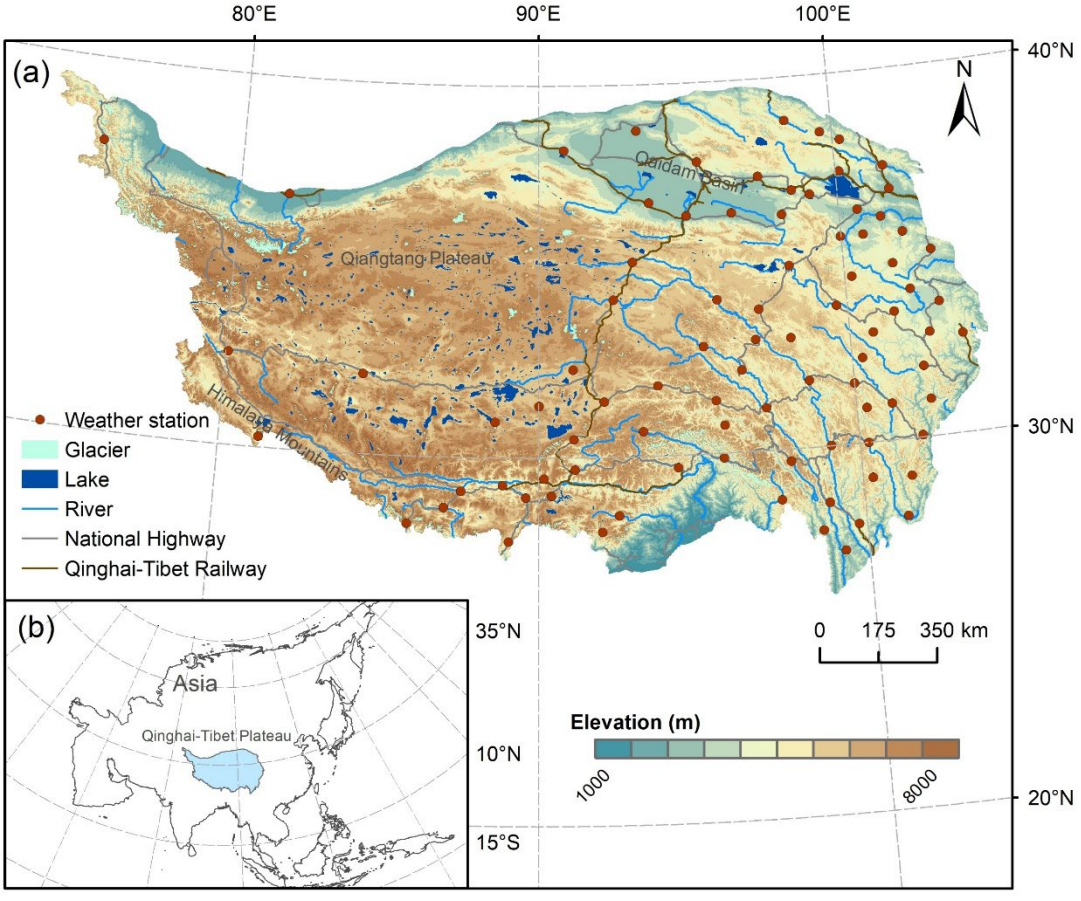

Figure 1 Topographic map and geographical context of the Qinghai-Tibet Plateau (QTP). (a) The topography of the region. The background color gradient represents elevation derived from the Shuttle Radar Topography Mission DEM. The 87 national meteorological stations (red dots) used for ground surface temperature correction, alongside major river systems and lakes are shown. (b) The location of the QTP in Asia.

2.2 Remote sensing and gridded datasets

2.2.1 Thermal forcing data

The primary drivers of permafrost thermal dynamics in our model are the freezing and thawing indices. To derive these indices, we utilized the Moderate Resolution Imaging Spectroradiometer (MODIS) LST products as the basis for estimating ground surface temperature (GST). We acquired the Version 6 Terra (MOD11A1) and Aqua (MYD11A1) daily LST products, which provide four observations per day at a 1 km spatial resolution.

To determine the permafrost distribution for the target year 2020, we processed data covering the five-year period from 2016 to 2020. This temporal selection satisfies the definition of permafrost (ground remaining frozen for at least two years) and minimizes the bias from interannual climate anomalies. Since the raw satellite skin temperatures differ from the ground surface thermal regime required by the model, these data were post-processed. This included a dedicated gap-filling procedure

https://doi.org/10.5194/egusphere-2026-345
Preprint. Discussion started: 4 March 2026

to address cloud contamination (Chen et al., 2023) and a subsequent LST-to-GST correction to account for the thermal buffering effects of vegetation and snow. The specific algorithms for these transformations are detailed in Sect. 3.2.

2.2.2 Data for estimating local soil parameter (*E*)

While regional thermal dynamics are driven by temperature indices, local permafrost occurrence is strongly modulated by surface and subsurface characteristics. In our model (Sect. 3.1), these local effects are aggregated into an empirical soil parameter *E*. To estimate *E*, we compiled environmental covariates representing topography, surface cover, soil properties, and moisture conditions (Karjalainen et al., 2019; Smith et al., 2022).

Topographic variables (slope, aspect, and topographic wetness index) were calculated from the Shuttle Radar Topography Mission (SRTM) 90 m Digital Elevation Model (DEM), which was aggregated to 1 km resolution to match the model grid. Surface cover conditions were characterized using the 1km, 16-day composite MODIS Normalized Difference Vegetation Index (NDVI) product (MOD13A2) and the daily 0.005° fractional snow cover (FSC) dataset over High Asia (Pan et al., 2024).

Subsurface thermal properties were represented by soil texture data (sand and clay fractions) extracted from the China Dataset of Soil Properties for Land Surface Modeling (Shangguan et al., 2013). Due to the lack of high-resolution soil moisture products, we utilized mean annual precipitation (MAP) as a proxy for regional soil moisture conditions, derived from the 1 km monthly precipitation dataset for China (Peng et al., 2019). All dynamic covariates (NDVI, FSC, and MAP) were averaged over the 2016–2020 period.

2.3 In situ observations

2.3.1 Meteorological station data

To correct the thermal offset between satellite-derived LST and the actual ground thermal regime, we utilized daily 0 cm GST observations from the Daily Meteorological Dataset of Basic Meteorological Elements of China National Surface Weather Station (1991-2020) (Zhao et al., 2024). The original dataset includes 131 stations across the QTP. We screened these stations based on the completeness of their data series, excluding sites with significant missing records during the 2016–2020 period. This selection process resulted in a final subset of 87 stations utilized for this study (Fig. 1). Daily GST records from 2016 to 2020 were extracted to correspond with the satellite acquisition period.

2.3.2 Borehole observations

Independent validation of the mapped permafrost distribution was conducted using a compilation of 109 borehole records. Due to the limited availability of deep ground temperature measurements coinciding exactly with 2020, we prioritized high-quality observations from the years immediately surrounding 2020, under the assumption that deep ground thermal states remain relatively stable over short timeframes. The primary data source was the comprehensive QTP permafrost thermal state synthesis by Zhao et al. (2021). From this dataset, we extracted records for 65 boreholes where ground temperatures were

https://doi.org/10.5194/egusphere-2026-345
Preprint. Discussion started: 4 March 2026

monitored at depths of 10 m and 20 m. We utilized the 2018 ground temperatures as the reference. Sites with MAGT < 0 °C at these depths were classified as permafrost.

To enhance spatial coverage, we integrated three regional datasets: (1) 32 boreholes from the Yangtze River Source area (Li et al., 2022) with direct presence/absence observations specifically for the year 2020; (2) 6 boreholes from the Yellow River Source area (Lei et al., 2024), classified using 2017 ground temperature profiles (0–20 m); and (3) 6 sites from the Heihe River Basin observation network (Mu et al., 2022) covering the northeastern QTP, all of which are situated in seasonally frozen ground (SFG) regions (based on records from 2011–2019). In total, the validation dataset comprises 83 confirmed permafrost sites and 26 seasonally frozen ground sites, providing a spatially diverse basis for accuracy assessment.

2.4 Existing permafrost datasets for comparison

To evaluate the accuracy of our new map, we utilized two existing permafrost datasets that provide simulations covering the year 2020. The first is the TTOP-based permafrost map (Yan et al., 2023). This map is derived from a long-term permafrost simulation dataset (1961-2020) generated at a 5-year interval using the TTOP model (Smith and Riseborough, 1996) driven by satellite LST and meteorological station observations. For this study, we extracted the permafrost distribution corresponding to the year 2020, which has a spatial resolution of 1 km.

The second is a MAGT-based permafrost map derived from a ground temperature simulation product (Zou et al., 2025). This dataset provides MAGT at a depth of 15 m for the period 2010–2019, generated using a Support Vector Machine model trained on records from 231 boreholes. For our comparison, grid cells with a 15 m ground temperature below 0 °C were classified as permafrost.

Additionally, we utilized glacier extent data from Ye et al. (2017) and 2020 lake boundaries from Zhang et al. (2021) to exclude non-soil areas from the analysis to ensure consistent land cover definitions across all maps.

3 Methodology

3.1 The extended FROSTNUM/COP model framework

To map the permafrost distribution for 2020, we applied the FROSTNUM model (Cao et al., 2023; Hu et al., 2020). This semi-physical approach, previously validated for the QTP by Cao et al. (2023), determines the probability of permafrost occurrence (frost number F) based on the balance between surface freezing and thawing loads, modulated by local ground properties. The frost number F is defined as:

$$F = \frac{\sqrt{DDF}}{\sqrt{DDF}+E\cdot\sqrt{DDT}}, \quad (1)$$

where DDF and DDT are the ground surface freezing and thawing indices ($°C \cdot d$), respectively. The parameter E is a dimensionless empirical factor that accounts for the local environmental modification of the ground thermal regime.

https://doi.org/10.5194/egusphere-2026-345
Preprint. Discussion started: 4 March 2026

Theoretically, E reflects the combined effects of soil thermal properties and moisture conditions in both frozen and thawed states. Based on this formulation, the threshold for permafrost occurrence is defined at $F > 0.5$. Pixels with $F \leq 0.5$ are classified as SFG or non-frozen ground.

A critical component of this framework is the determination of E. In the original methodology established (Cao et al., 2023; Hu et al., 2020), the E parameter was retrieved via an inverse optimization strategy that minimized the error between the model output and extensive concurrent field survey maps. This ensured that the 2010 map accurately reflected the specific ground conditions of that year. However, a direct application of this original optimization strategy is not feasible for 2020. This process relies strictly on the availability of concurrent permafrost distribution maps for calibration, which do not exist for the year 2020. To overcome this limitation, this study introduces a novel adaptation. We hypothesize that while the specific value of E at a given location may shift due to changes in moisture or surface cover, the fundamental statistical relationship between E and its environmental drivers (such as topography, vegetation, soil texture, soil moisture) remains applicable over the decadal scale. Consequently, we employ a space-for-time substitution strategy to predict the 2020 E field based on the relationships learned from the high-quality 2010 dataset (Fig. 2).

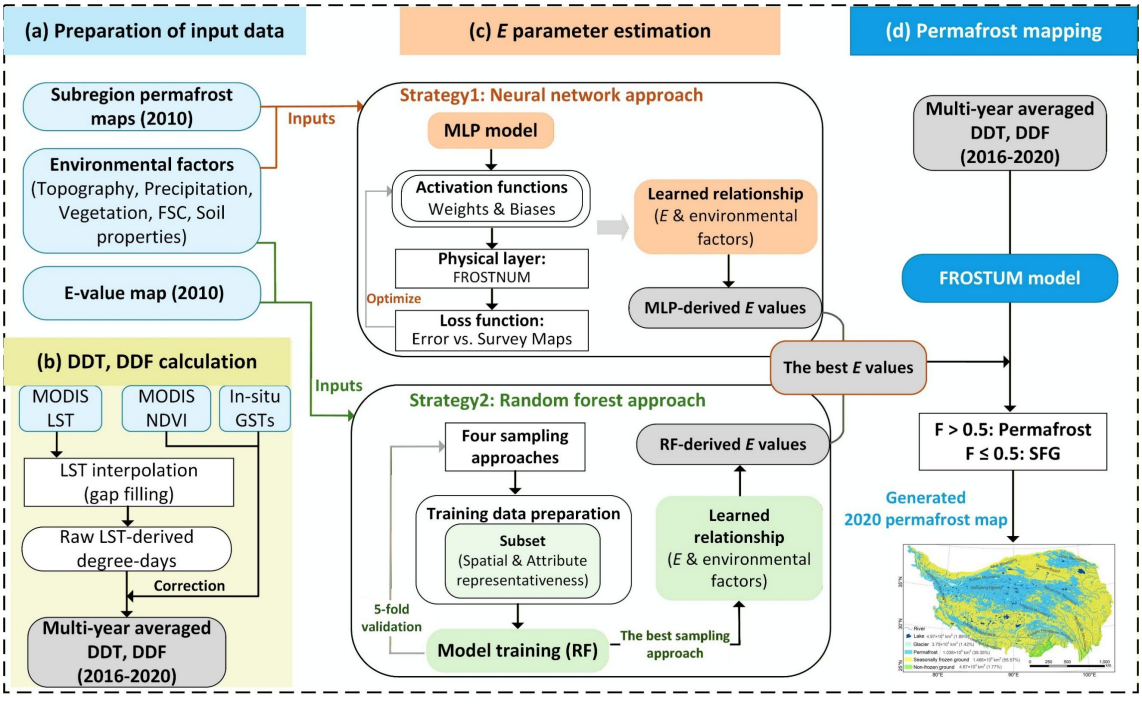

Figure 2 Schematic flowchart of the methodology to map the 2020 permafrost distribution. The workflow comprises four distinct stages: (a) Preparation of multi-source input datasets, including satellite forcing data and environmental covariates; (b) Calculation of ground surface freezing (*DDF*) and thawing (*DDT*) indices from gap-filled MODIS land surface temperature (LST), corrected to represent ground surface conditions; (c) Estimation of the empirical soil parameter *E* via a space-for-time substitution strategy. This stage compares two transfer learning approaches: a neural network (MLP) approach and a Random Forest (RF) regression with optimized spatial sampling; and (d) Final permafrost distribution mapping using the extended ground surface frost number model (FROSTNUM). FSC: fractional snow cover; MODIS (Moderate Resolution Imaging Spectroradiometer); GST: ground surface temperature; NDVI: normalized difference vegetation index; SFG: seasonally frozen ground; and MLP: multilayer perceptron model.

https://doi.org/10.5194/egusphere-2026-345
Preprint. Discussion started: 4 March 2026

3.2 Calculation of ground surface freezing and thawing indices

The driving variables for the model, the ground surface freezing and thawing indices (*DDF* and *DDT*), were derived from the daily MODIS LST products (MOD11A1 and MYD11A1) covering the 2016–2020 period. The processing workflow comprised gap-filling, daily aggregation, and the correction from LST to GST. Due to frequent cloud cover on the QTP, raw MODIS LST data suffer from extensive gaps. We addressed this using the solar-cloud-satellite geometry interpolation method developed by Chen et al. (2023). This approach reconstructs missing pixels by leveraging the geometric relationship between the sun, cloud position, and satellite view angle, ensuring high-accuracy all-weather LST estimates. Following gap-filling, the daily mean LST was calculated from the four daily instantaneous observations (two daytime and two nighttime) using a sinusoidal integration method (van Doninck et al., 2011).

Based on the gap-filled daily mean LST series, the raw surface freezing and thawing indices were computed. The freezing index (*DDF*) was calculated as the annual sum of negative degree-days. For the thawing index (*DDT*), a correction was necessary to account for the thermal offset between the satellite-observed LST and the actual GST, primarily caused by the insulating effect of vegetation during the growing season. Consistent with Cao et al. (2023), we corrected the LST-derived *DDT* using multilinear regression model (Eq. (2)) that incorporates vegetation greenness and latitude. The correction is applied at 16-day intervals (corresponding to MODIS NDVI composites) to derive a final annual DDT_{GST}:

$$DDT_{i,GST} = f\left(DDT_{i,LST}, \mathrm{NDVI}_i, Lat\right), \quad (2)$$

where $DDT_{i,GST}$ represents the corrected ground surface thawing degree-days ($°C \cdot d$) for the *i*-th temporal interval (corresponding to the 16-day MODIS composites period); $DDT_{i,LST}$ is the raw thawing degree-days accumulated from positive daily mean LST values during the same *i*-th interval, $NDVI_i$ is corresponding NDVI value, serving as a proxy for vegetation density and its thermal insulating capacity; and *Lat* is the geographic latitude, which accounts for regional variations in solar radiation and incidence angle. We did not apply correction to the freezing index (*DDF*), as snow cover on the QTP is thin, ephemeral, spatially discontinuous, which results in a negligible insulation effect at the regional scale (Wu and Zhang, 2008; Zhao et al., 2017).

3.3 Estimation of soil parameter *E* via space-for-time substitution

We implemented a space-for-time substitution strategy to obtain *E* for 2020 without concurrent field surveys. This methodological paradigm is widely established in Earth system sciences, particularly in climatology, atmospheric modeling, and ecology, where spatial gradients are frequently utilized to infer temporal dynamics or to parameterize processes in data-scarce scenarios (Huang et al., 2019; Pickett, 1989). In the context of this study, the approach relies on the hypothesis that while the specific value of *E* at a location may shift due to changes in moisture or surface cover, the fundamental statistical dependencies between *E* and environmental covariates (soil texture, topography, and vegetation-moisture proxies) observed in 2010 remain valid for predicting the 2020 state. To implement this, we developed and compared two distinct transfer learning strategies, each prioritizing a different source of training data. Both strategies utilized the same suite of predictors to estimate

https://doi.org/10.5194/egusphere-2026-345
Preprint. Discussion started: 4 March 2026

E, specifically: topographic variables (elevation, slope, aspect, TWI), soil texture (sand and clay fractions), vegetation conditions (NDVI), snow cover (FSC), and precipitation (MAP).

The first strategy aimed to learn the *E*-environment relationship directly from the high-reliability field survey maps available for five sub-regions in the 2010 study. We constructed a hybrid physics-informed neural network (Fig. 2c). This architecture integrates a Multi-Layer Perceptron (MLP) (Fu et al., 2025; Park and Lek, 2016) with the physical FROSTNUM model in an end-to-end differentiable framework. In the forward pass, the MLP predicts the local parameter *E* from environmental inputs, which is immediately passed through the differentiable FROSTNUM layer to calculate the frost number and subsequent binary classification. In the backward pass, the generated classification is compared directly against the survey maps, and the classification error is backpropagated through the physical layer to update the MLP weights.

The second strategy prioritized spatial continuity and statistical robustness by utilizing the full 2010 *E*-field, retrieved via the original Clustering-Optimization-Prediction procedure (Cao et al., 2023), as the training target. Unlike the first strategy, which relied on sparse survey data, this approach treated the estimation as a direct regression problem using the spatially continuous 2010 baseline map. While the original study aggregated the plateau into eight parameter clusters, we expanded this to sixteen classes for the training target. This refinement was necessary because restricting the target variable to only eight discrete values lose the continuous nature of the variable, thus limiting the RF's ability to learn subtle environmental gradients. We trained a RF model (van Der Westhuizen et al., 2023; Wadoux et al., 2019) to learn the relationships between the environmental covariates and these "observed" *E* values.

Crucially, for the second strategy, we implemented a representative sampling framework to select the training data. Given the high spatial heterogeneity of the QTP, simple random sampling often fails to capture rare but physically significant parameter combinations, leading to high predictive uncertainty. We evaluated four distinct sampling techniques: *k*-means clustering sampling (Brus et al., 2006), Equal Range (ER) sampling (Hengl et al., 2003), Principal Component Analysis (PCA)-based sampling (Hengl et al., 2003), and Latin Hypercube Sampling (LHS) (Carré et al., 2007) across four different sample sizes (1000, 3000, 5000, and 10000 points). We aimed not only to improve computational efficiency and reduce information redundancy but, more importantly, to minimize the uncertainty associated with the *E*-value distribution. Detailed mathematical formulations and implementation procedures for these four sampling strategies are provided in Appendix A. The optimal configuration, determined via 5-fold cross-validation, and the superior strategy selected from this comparison was used to drive the final FROSTNUM simulation for the 2020 permafrost map.

3.4 Validation

The accuracy and reliability of the generated 2020 permafrost map were evaluated through a multi-tiered validation framework designed to assess both the intermediate modeling steps and the final spatial product. First, to determine the optimal transfer learning strategy for estimating the soil parameter *E*, we conducted a rigorous comparative evaluation of the MLP and the RF strategies described in Sect. 3.3. For the RF approach, we utilized 5-fold cross-validation to assess its ability to reproduce the 2010 baseline values, quantifying performance using the Correlation Coefficient (*r*), Mean Absolute Error

https://doi.org/10.5194/egusphere-2026-345
Preprint. Discussion started: 4 March 2026

(MAE), Root Mean Square Error (RMSE), and percentage of variance explained. For the MLP approach, the MLP performance was validated indirectly by assessing the classification accuracy of the simulated permafrost distribution in the target subregions. Specifically, we randomly selected 70% of the pixels within these subregions for training, while the remaining 30% were reserved for validation. We also assessed the spatial consistency of the MLP-derived permafrost distribution for 2010 by comparing it with the benchmark permafrost map from Cao et al. (2023).

Second, we performed a dual-facet validation focusing on both the accuracy of the 2020 map and the plausibility of the detected temporal changes. The spatial accuracy of the resulting 2020 permafrost distribution (generated using the selected optimal strategy) was rigorously assessed against the independent dataset of 109 borehole records. To perform this evaluation, we extracted the simulated permafrost status (permafrost or SFG) at the coordinates of each borehole and compared it with the in-situ ground truth. Beyond static accuracy, we also verified the reasonableness of the simulated permafrost changes between 2010 and 2020 using 0 cm GST data from meteorological stations and available field evidence.

Additionally, to assess the map's consistency with current regional knowledge, we performed a spatial inter-comparison with two existing datasets covering the same period: the TTOP-based simulation by Yan et al. (2023) and the data-driven ground temperature map by Zou et al. (2025). We analyzed the agreement in permafrost area and spatial distribution patterns, specifically quantifying discrepancies in the zones where modeling uncertainty is typically highest. Finally, to further diagnose the physical drivers underlying these shifts, we conducted a comparative analysis of key environmental and thermal variables by comparing their values in the changed areas versus adjacent unchanged regions.

4 Results

4.1 Spatiotemporal changes in thermal forcing

The thermal forcing indices driving the permafrost model exhibited distinct spatial shifts between the 2010 baseline and the 2020 target period. The ground surface thawing index (*DDT*), corrected to account for the thermal offset between satellite-observed skin temperature and the actual ground surface, revealed a spatially divergent pattern (Fig. 3a-c). As shown in the difference map (Fig. 3c), significant warming persisted in the arid northern Qaidam Basin and the western Qiantang Plateau, where sparse vegetation offers limited thermal buffering. In sharp contrast, a notable cooling trend was observed in the eastern QTP, particularly within the Three-River Headwater region. The localized cooling is likely attributable to the greening of the plateau, a phenomenon well-documented in the southeastern QTP over recent decades (Shi et al., 2023; Wang et al., 2022). Vegetation modulates the surface energy budget through three primary mechanisms: (1) reducing aerodynamic resistance and enhancing latent heat flux via evapotranspiration; (2) increasing soil water retention, which raises the thermal inertia of the soil; and (3) providing direct insulation that delays the onset of active-layer thaw (Jia et al., 2023; Ni et al., 2025; Wang et al., 2012). Collectively, these processes appear to have dampened, or even reversed, the ground thermal response to rising air temperatures in the eastern plateau.

https://doi.org/10.5194/egusphere-2026-345
Preprint. Discussion started: 4 March 2026

In parallel, the freezing index (*DDF*) reflected these regional climatic contrasts (Fig. 3 d-f). Between 2010 and 2020, pronounced winter warming (manifested as reduced *DDF* in Fig. 3f) occurred across the central QTP and was particularly intense along the southern Himalayan margin. Conversely, localized cooling (increased *DDF*) was observed in the western QTP and the eastern mountainous regions (Fig. 3f). As a result, the *DDT*-to-*DDF* ratio (*DDT*/*DDF*), a key climatic indicator of permafrost stability, increased markedly across the majority of the QTP from 2010 to 2020 (Fig. 3g-i). This positive shift signals a climate trajectory unfavorable for permafrost preservation in these regions. However, the eastern region showed a decrease in the *DDT*/*DDF* ratio, consistent with the observed *DDT* and *DDF* cooling trend.

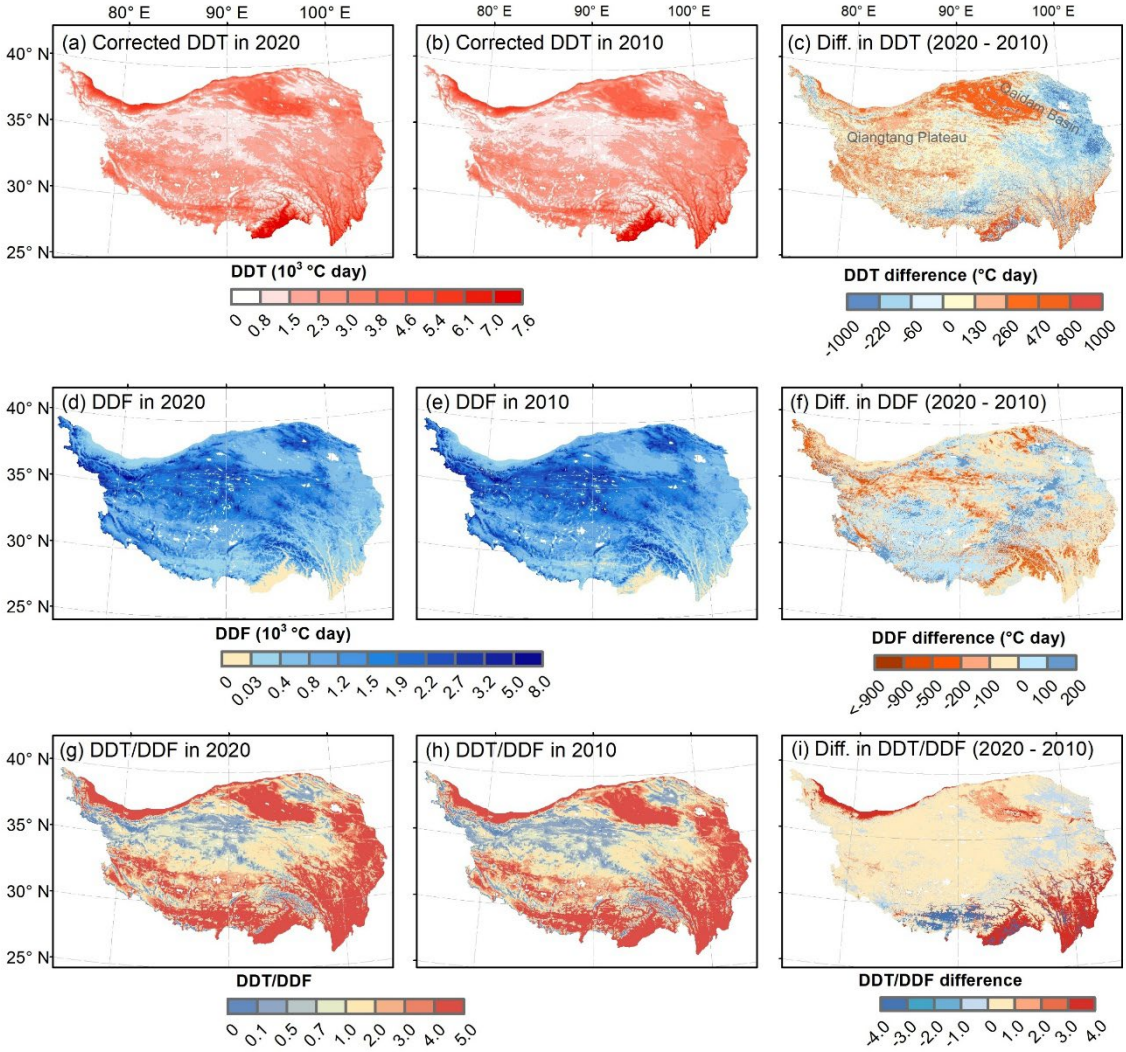

Figure 3 Spatial distribution and decadal changes of thermal forcing indices on the QTP. (a-c) displays the ground surface thawing index (and decadal change of *DDT*), (d-f) the freezing index, and (g-i) the ratio of thawing to freezing indices. Left column shows the distributions in 2020, middle column shows the distributions in 2010, and the right column shows the differences between 2020 and 2010. For (c) and (i), positive values (red) indicate warming/instability, while negative values (blue) indicate cooling/stability. For (f), negative values (red) indicate winter warming (reduced freezing), while positive values (blue) indicate cooling.

https://doi.org/10.5194/egusphere-2026-345
Preprint. Discussion started: 4 March 2026

4.2 Estimation of the soil parameter *E* for 2020

To spatially extrapolate the empirical soil parameter *E* to 2020, we evaluated the generalization capabilities of two distinct transfer learning strategies: the MLP approach and the RF approach. The comparison revealed a critical trade-off between model complexity and predictive stability. The MLP model achieved a high prediction accuracy (95.26%) within the training subregions. However, when applied to the plateau-wide domain, the model exhibited severe overfitting, likely due to the equifinality inherent in training against binary classification data without sufficient physical constraints. The MLP-predicted *E* field was characterized by unrealistic spatial artifacts, with clustering narrowly near zero or scattering across implausible magnitudes (see Appendix B). Crucially, when we utilized this MLP-derived *E* field to reconstruct the permafrost distribution for 2010, the resulting map deviated significantly from the rigorously validated benchmark established by Cao et al. (2023). This failure likely stems from the "black box" nature of deep learning, which, in this context, lacked effective physical constraints and consequently suffered from poor generalization capability.

In contrast, the RF-based strategy demonstrated superior robustness and spatial coherence. Among the four sampling strategies evaluated, the *k*-means clustering sampling approach (utilizing 5000 points) produced the optimal performance, achieving the lowest RMSE (0.048) and highest correlation coefficient (r= 0.862) against the 2010 baseline (Table 1). Visual inspection confirmed that the RF-derived field successfully reproduced the complex heterogeneity of soil properties across the QTP (Fig. 4a). Therefore, the RF-derived predictions were adopted for the final permafrost mapping.

Based on the RF simulations, the spatial distribution of *E* in 2020 exhibited significant shifts relative to 2010. We categorized areas into a "Positive group" (increased *E*, indicating higher degradation risk) and a "Negative group" (decreased *E*, indicating reduced risk). The analysis shows that the area of the Positive group (55% of the total changed area) exceeded that of the Negative group (45%), suggesting a dominance of processes conducive to permafrost degradation (Fig. 4c).

Table 1 Comparison of the predictive accuracy of four sampling strategies for estimating the local soil parameter *E*. Accuracy metrics (RMSE, MAE, *r*, and % variance explained) are derived from 5-fold cross-validation using an optimal sample size of 5000 points.

Sampling method	RMSE	MAE	r	% variance explained
k-means sampling	0.048	0.029	0.862	74.83
Equal Range (ER) sampling	0.049	0.030	0.831	69.18
PCA-based sampling	0.049	0.030	0.831	69.90
Latin Hypercube Sampling (LHS)	0.054	0.036	0.806	65.74

https://doi.org/10.5194/egusphere-2026-345
Preprint. Discussion started: 4 March 2026

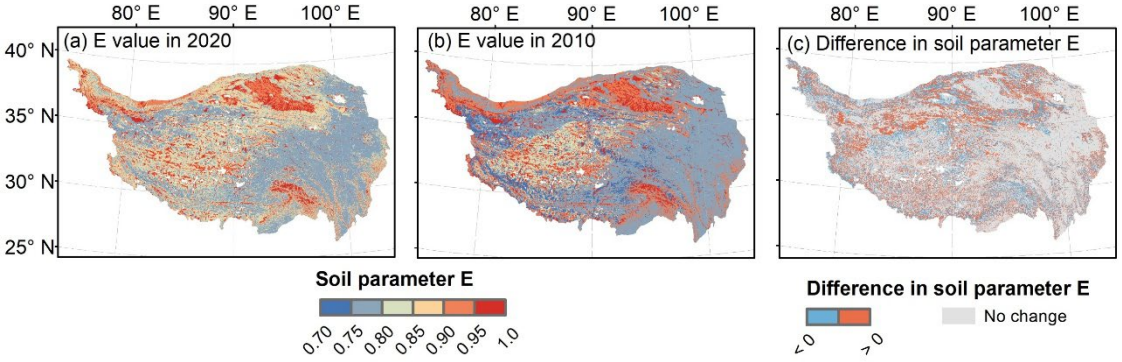

Figure 4 Spatial distribution of the soil parameter *E* in 2020 (a) and 2010 (b). (c) illustrates the difference (2020 minus 2010), where positive values (red) indicate an increase in *E* (conditions conducive to degradation) and negative values (blue) indicate a decrease.

To elucidate the physical mechanisms driving these shifts in *E*, we analyzed the temporal variations of the environmental predictors (Fig. 5). While vegetation indices (NDVI) (Fig. 5b) and snow cover (FSC) (Fig. 5c) showed uniform increases across both groups, precipitation emerged as the distinct driver of divergence (Fig. 5d). It is important to note that due to the lack of high-resolution soil moisture products for the region, mean annual precipitation is utilized here as a proxy for regional soil moisture conditions. Although the QTP experienced a general wetting trend (Zhang et al., 2021), the regions characterized by increasing *E* (positive group) received significantly less precipitation increase (+1.28 mm median increase) compared to the Negative group (+2.23 mm median increase). This relative moisture deficit has profound thermal implications. Soil moisture acts as a crucial thermal buffer due to the high specific heat capacity and latent heat of fusion of water. A smaller increase in precipitation implies relatively drier soil conditions in the positive group, resulting in reduced soil thermal inertia. Consequently, these soils are more responsive to atmospheric warming, leading to a higher *E* value and an accelerated thawing process.

https://doi.org/10.5194/egusphere-2026-345
Preprint. Discussion started: 4 March 2026

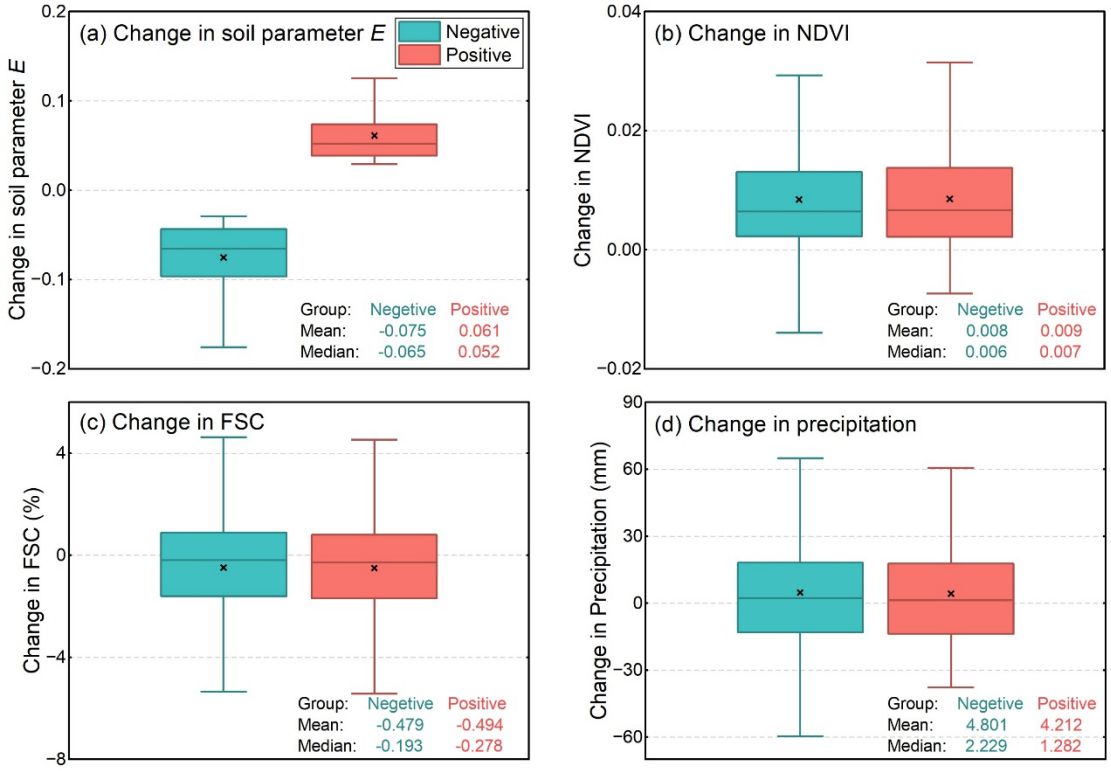

Figure 5 Distribution of decadal changes (2010-2020) in key environmental factors, categorized by the trend in soil parameter *E*. Boxplots compare changes in (a) soil parameter *E*, (b) NDVI, (c) FSC and (d) precipitation between regions of increased risk (positive group) and reduced risk (negative group). In each box plot, the center line shows the median, the box represents the lower and upper quartiles (25th-75th percentiles), and the whiskers extend to the furthest data points within 1.5 times the interquartile range. The 'x' marks the mean.

4.3 The 2020 permafrost distribution map

The final permafrost distribution map for 2020, generated using the optimized RF-derived *E* parameter and corrected thermal forcing indices, is presented in Fig. 6. Statistical analysis shows that permafrost covers approximately 1.038×10^6 km^2, accounting for 39.35% of the total QTP area (excluding lakes and glaciers). SFG region is the dominant frozen ground type, occupying 1.466×10^6 km^2 (55.57%), while non-frozen ground is restricted to the lowest marginal valleys (1.77%, 4.67×10^4 km^2).

The spatial pattern of the 2020 map exhibits a strong altitudinal and latitudinal zonality consistent with the region's topoclimatic gradients. The most extensive continuous permafrost body is concentrated in the high-elevation interior, encompassing the Qiangtang Plateau, the Hoh Xil region, and the Bayan Har Mountains. The combination of extreme elevation (>4500 m) and the arid, continental climate maintains a stable negative ground thermal regime. This continuous zone acts as the cold core of the plateau, interrupted only by large endorheic lakes which form localized taliks. To the north, the Qaidam Basin creates a distinct break in the permafrost continuity. Despite its high latitude, the basin's significantly lower elevation

https://doi.org/10.5194/egusphere-2026-345
Preprint. Discussion started: 4 March 2026

and distinctive arid-desert thermal regime preclude permafrost formation, creating a vast expanse of SFG that physically isolates the permafrost of the Qilian Mountains from the main plateau body. The Qilian permafrost thus exists as a large-scale "island" system, maintained strictly by the orographic uplift of the mountain range.

Moving southward and eastward from the Qiangtang core, the permafrost distribution becomes increasingly fragmented. In the eastern QTP, particularly in the Three-River Headwater Region, the landscape is dominated by SFG, with permafrost confined to high ridges. This distribution is likely modulated by the advective heat transport from the developed river networks and the relatively lower latitude, rendering the permafrost in this region thermally fragile (Zhang et al., 2022). Similarly, along the southern and southeastern margins (the Himalayas, the Gangdise Mountains, and the Hengduan Mountains), the permafrost distribution is strictly topographically controlled. In these regions, the combination of lower latitude and deeply dissected terrain creates sharp thermal gradients. Permafrost is discontinuously distributed, clinging to the high-altitude ridgelines and islands of extreme elevation, while the deep, incised valleys maintain non-frozen ground or SFG.

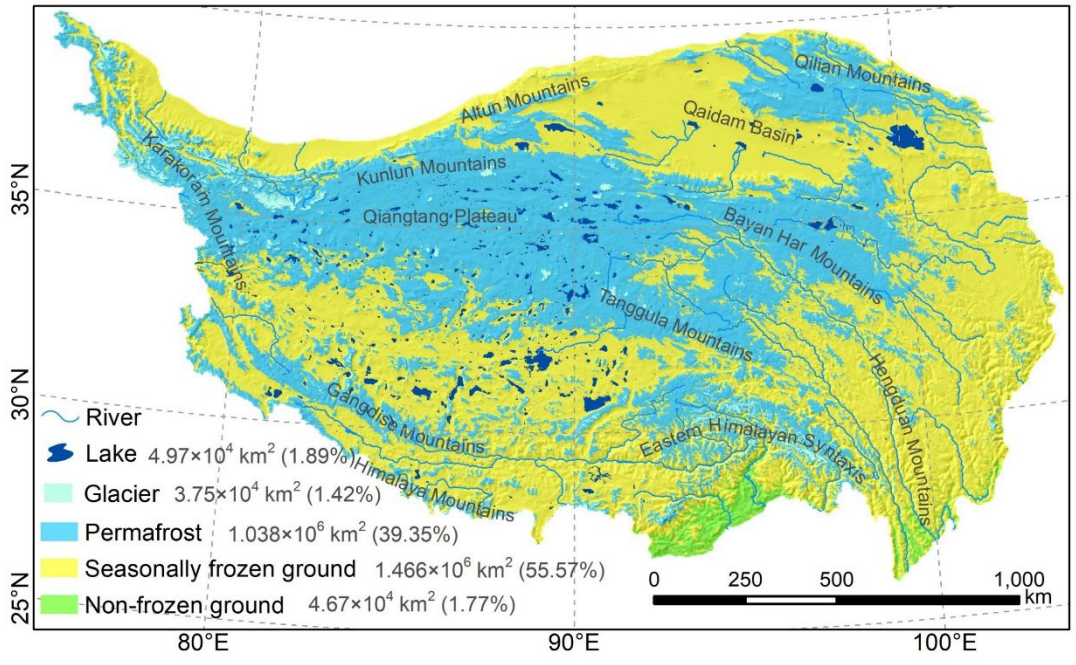

Figure 6 Map of frozen ground distribution at 1 km resolution over the QTP in 2020. Areas and percentages of frozen soil types are present.

https://doi.org/10.5194/egusphere-2026-345
Preprint. Discussion started: 4 March 2026

4.4 Accuracy assessment and inter-comparison

4.4.1 Validation against borehole observations

Quantitative validation was performed using 109 independent borehole records from the 2020 period (Table 2). Our map achieved an overall accuracy of 84.4% and a Cohen's Kappa coefficient of 0.58, outperforming both the MAGT-based map (81.7%, $\kappa = 0.38$) and the TTOP-based map (78.9%, $\kappa = 0.28$).

A critical advantage of our approach lies in its balanced classification capability. While both reference maps exhibited high sensitivity, identifying over 90% of confirmed permafrost sites, they suffered from significant commission errors, frequently misclassifying SFG as permafrost. In contrast, our map demonstrated a superior ability to differentiate SFG, achieving a true negative rate of 69.2%, compared to just 34.6% for the MAGT-based map and 42.3% for the TTOP-based map. This substantial improvement indicates that our method effectively mitigates the overestimation of permafrost extent that is prevalent in existing simulations.

https://doi.org/10.5194/egusphere-2026-345
Preprint. Discussion started: 4 March 2026

Table 2 Confusion matrix describing the performance of the evaluated permafrost maps (Our map, MAGT-based map and TTOP-based map) against 109 borehole validation sites

	Our map	MAGT-based map	TTOP-based map
Overall Accuracy	84.4%	81.7%	78.9%
Cohen's Kappa	0.58	0.38	0.28
True positive rate (permafrost)	74 (89.2%)	80 (96.4%)	75 (90.4%)
True negative rate (SFG)	18 (69.2%)	9 (34.6%)	11 (42.3%)
False positive rate	8 (30.8%)	17 (65.4%)	15 (57.7%)
False negative rate	9 (11.8%)	3 (3.6%)	8 (9.6%)

4.4.2 Spatial inter-comparison

To further verify the map's physical realism, we analyzed spatial inconsistencies between our results and the reference maps in distinct subregions (Fig. 7), specifically focusing on transition zones where modelling uncertainty is typically high. Significant discrepancies were observed in these areas, where ground observations consistently supported our simulation over the reference datasets.

In the Gaize area (subregion a in Fig. 7a, b) both reference maps failed to identify the seasonally frozen status of borehole ZK043 (Fig. 8a, Fig. 9a), whereas our map correctly classified it as SFG. Additionally, our map correctly identified borehole ZK042 as SFG, a site also situated in this transition zone. In the northern marginal zone between the Altun and Kunlun Mountains (subregion b in Fig. 7a), ground observations indicate the presence of four SFG boreholes (Fig. 8b). Our map correctly recognized all four, whereas the MAGT-based map identified only one (Fig. 8b). Although our simulation classified two confirmed permafrost boreholes in this region as SFG (Fig. 8b), observational records indicate these sites possessed extremely warm MAGT of -0.13 °C in 2013-2016 and -0.17 °C in 2013-2018. Such values characterize thermally unstable permafrost highly susceptible to degradation, suggesting that our map likely reflects a recent transition to SFG that the historical baseline of the borehole predates.

Further discrepancies were identified in the headwaters of the Yangtze River (subregion c in Fig. 7a, b). Here, our map correctly identified four out of five confirmed SFG boreholes, whereas the MAGT-based map identified only one (Fig. 8c) and the TTOP-based map identified three (Fig. 9b). While our simulation misclassified three confirmed permafrost boreholes in this region as SFG (Fig. 8c), it is important to note that these sites are situated within a permafrost transition zone where MAGTs range from -0.37 °C to -0.48 °C. These close to zero values suggest that the classification discrepancy may reflect real-world degradation or the inherent uncertainty in modeling such marginal thermal states. Crucially, meteorological station 56004 in this area was classified as permafrost by both reference maps but as SFG by ours (Fig. 8c, Fig. 9b). Analysis of in-situ GST (0cm) data (2016-2019) at this site revealed a thawing index ($DDT \approx 2004\ °C \cdot d$) significantly exceeding the freezing index ($DDF \approx 1332\ °C \cdot d$). Since a thawing index exceeding the freezing index is robust indicator of SFG, this observation provides strong evidence that our simulation offers a more reliable representation of the current thermal regime.

https://doi.org/10.5194/egusphere-2026-345
Preprint. Discussion started: 4 March 2026

In the headwaters of the Yellow River (subregion d in Fig. 7a), the SFG borehole XXH-1 was correctly classified by our map but was misclassified as permafrost by the MAGT-based map (Fig. 8d). Although notable spatial inconsistencies were also observed along the southern margin of the plateau (subregion e in Fig. 7b), this area was excluded from the detailed inter-comparison due to the lack of available borehole observations for validation.

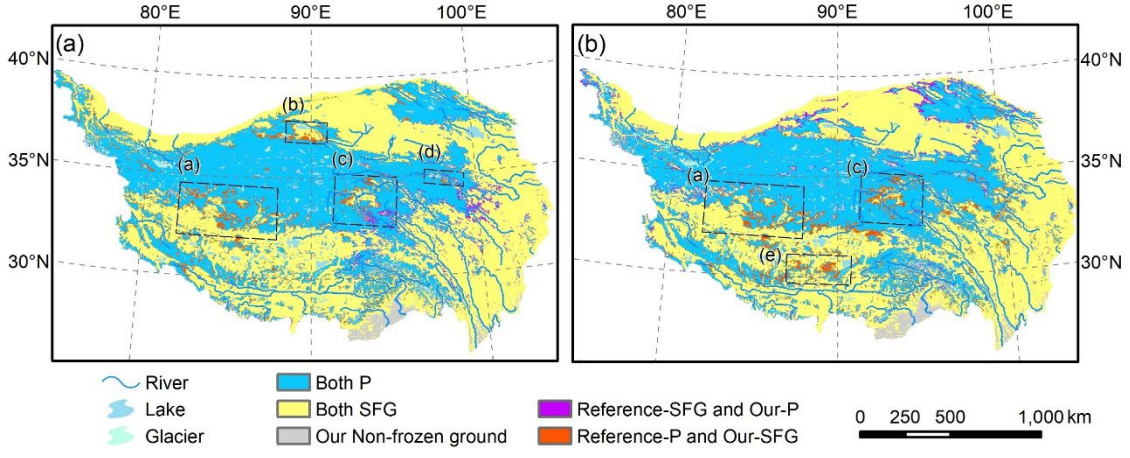

Figure 7 Spatial inconsistencies in the distribution of frozen ground between the generated 2020 permafrost map and reference datasets: (a) the Mean Annual Ground Temperature (MAGT) based map (Zou et al., 2025) and (b) the Temperature at the Top of Permafrost (TTOP) based map (Yan et al., 2023). "Both P" (blue) and "Both SFG" (yellow) denote consistent classification. "Reference-P and Our-SFG" represents regions classified as permafrost by the reference map but as SFG in our map. "Reference-SFG and Our-P" indicate the opposite. The dashed boxes mark specific transition zones with obvious inconsistency: (a) Gaize and its vicinity, (b) the Altun–Kunlun Mountains transition zone, (c) the headwaters of the Yangtze River, (d) the headwaters of the Yellow Rive, and (e) the southern margin.

https://doi.org/10.5194/egusphere-2026-345
Preprint. Discussion started: 4 March 2026

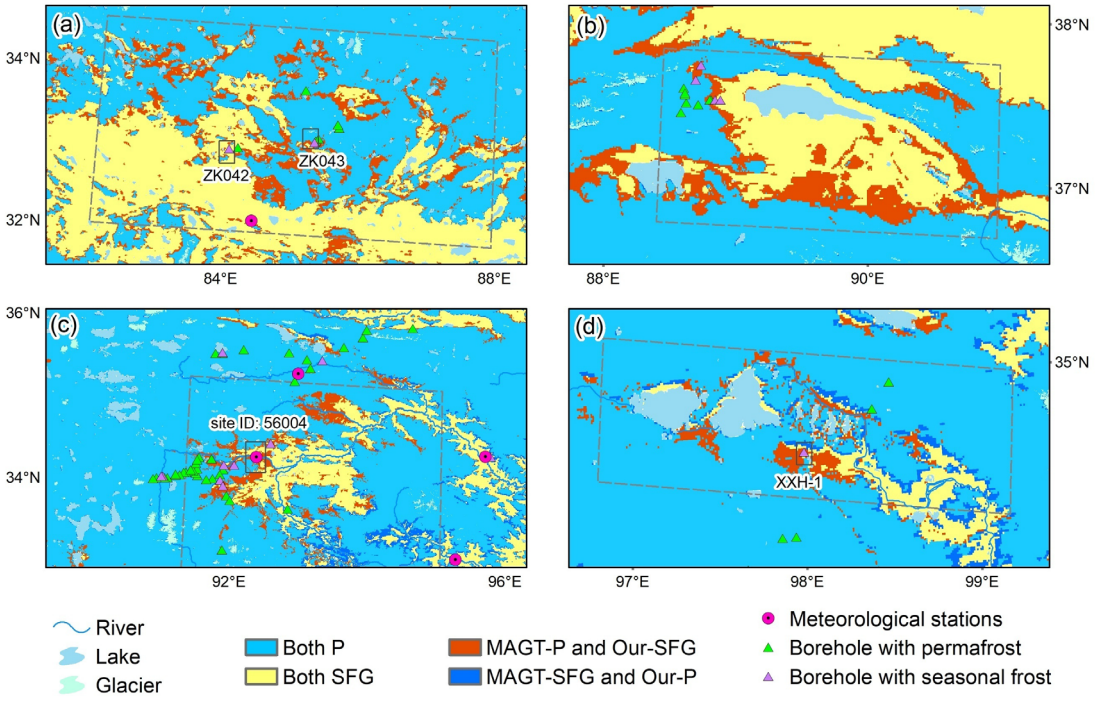

Figure 8 Detailed validation of spatial inconsistencies between the generated 2020 map and the MAGT-based map using ground-truth observations. The panels (a)-(d) correspond to the four subregions outlined in Fig. 7a. "MAGT-P and Our-SFG" represents regions classified as permafrost by the MAGT-based map but as SFG by our map. "MAGT-SFG and Our-P" indicates the opposite.

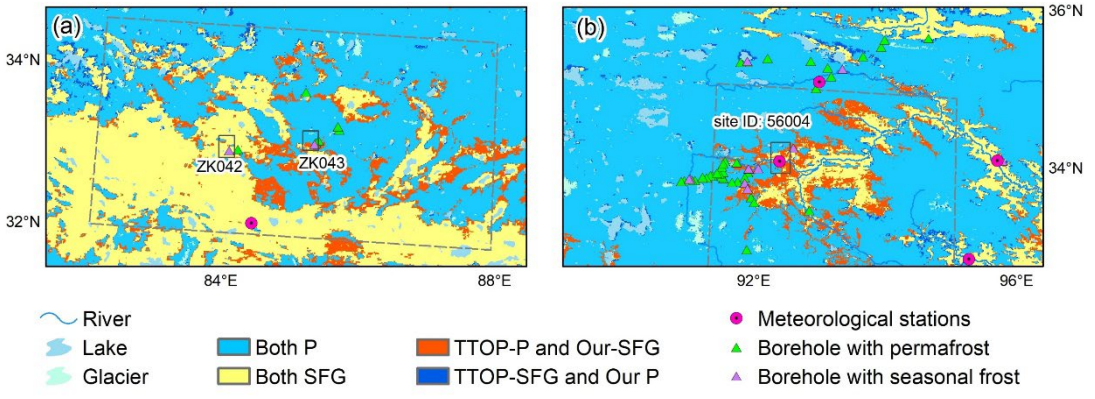

Figure 9 Detailed validation of spatial inconsistencies between the generated 2020 map and the TTOP-based map in two key transition zones. Panels (a) and (b) correspond to the subregions (a and c) outlined in Fig. 7b. "TTOP-P and Our-SFG" indicates areas identified as permafrost by the TTOP-based map but as SFG by our map. "TTOP-SFG and Our-P" indicates the opposite.

https://doi.org/10.5194/egusphere-2026-345
Preprint. Discussion started: 4 March 2026

4.5 Decadal changes in frozen ground distribution (2010–2020)

Between 2010 and 2020, the frozen ground distribution on the QTP underwent a distinct phase of degradation (Fig. 10), characterized by a net loss of permafrost extent and a concurrent expansion of SFG and non-frozen ground (Fig. 10a). Spatially, these shifts were not uniform but exhibited a clear bifurcation between the plateau's interior and its margins. Quantitative analysis indicates that the total permafrost area decreased by approximately 4.8×10^4 km^2 over the decade, representing a decline of 1.82% relative to the total area (Table 3). This loss was primarily driven by the conversion of unstable permafrost into SFG. Consequently, the SFG area expanded by 1.9×10^4 km^2 (a 0.72% increase). More strikingly, the area of non-frozen ground increased by 2.43×10^4 km^2 (a 0.92% increase), reflecting a significant range contraction of the frozen ground domain at its lower elevational and latitudinal limits.

The spatial evolution of these transitions reveals two dominant degradation patterns. In the central QTP region (subregion a in Fig. 10b), continuous or discontinuous alpine permafrost degraded into SFG. This process accounted for 7.41% of the total changed area and was largely concentrated in the transitional zones of the Qiangtang Plateau. Conversely, the southern and southeastern margins (subregion b in Fig. 10b), particularly the flanks of the Hengduan, Himalayan, and Gangdise mountains, experienced marginal retreat. The dominant transition was the conversion of SFG to non-frozen ground, which accounted for 39.62% of the total changed area (Fig. 10b). This shift indicates a vertical ascent of the frozen ground lower limit in response to warming. Beyond the ground thermal state, surface hydrological and glaciological features also responded to the warming climate. During this period, the glacier area decreased by 0.33×10^4 km^2 (Ye et al., 2017), while the lake area expanded by 0.80×10^4 km^2 (Zhang et al., 2021) (Table 3), consistent with the broader warm-wet climate trend observed across the region.

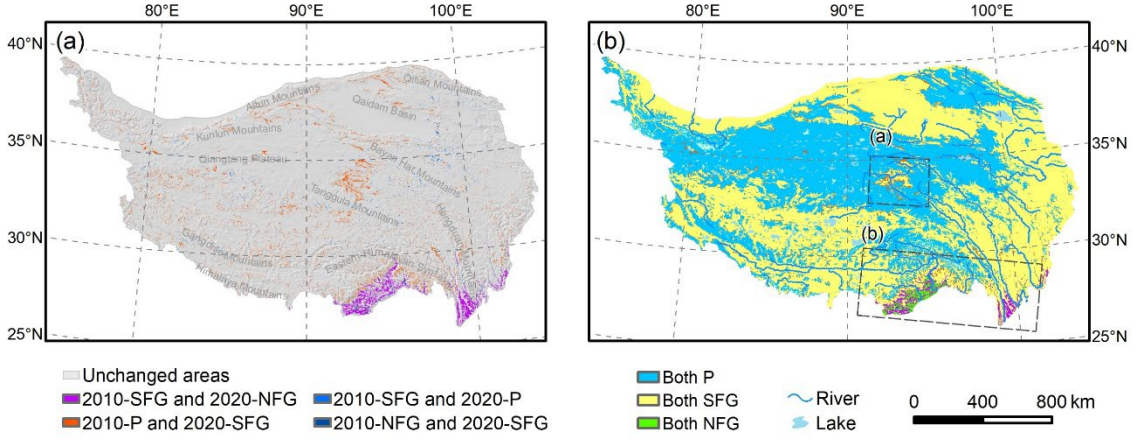

Figure 10 Spatiotemporal evolution of frozen ground types on the QTP from 2010 to 2020. (a) The spatial distribution of transition types overlaid on a hillshade map. (b) The same transitions shown against the background of the 2010 permafrost distribution. The rectangles delineate two hotspots of significant change: subregion a (central QTP) and subregion b (southern QTP).

https://doi.org/10.5194/egusphere-2026-345
Preprint. Discussion started: 4 March 2026

Table 3 Areas and decadal changes for different frozen ground types, glaciers, and lakes on the QTP from 2010 to 2020. Absolute areas are provided in km^2, with percentages of the total areas shown in parentheses.

	Permafrost	SFG	Non-frozen	Glacier	Lake
2010	1.086×10^6	1.447×10^6	2.24×10^4	4.08×10^4	4.17×10^4
	(41.17 %)	(54.85%)	(0.85%)	(1.55%)	(1.58%)
2020	1.038×10^6	1.466×10^6	4.67×10^4	3.75×10^4	4.97×10^4
	(39.35%)	(55.57%)	(1.77%)	(1.42%)	(1.89%)
Difference	-4.8×10^4	1.9×10^4	2.43×10^4	0.33×10^4	0.80×10^4
	(1.82%)	(0.72%)	(0.92%)	(0.13%)	(0.31%)

4.6 Mechanisms driving permafrost degradation

We conducted a targeted analysis of the two identified hotspots (subregion a, b in Fig. 10b). In the central QTP (Fig. 11a), the dominant process was the degradation of permafrost into SFG. This region corresponds to a critical transition zone where the permafrost is inherently warm and sensitive to thermal perturbations (Zhang et al., 2022). The spatial pattern of our simulated degradation exhibits a strong correspondence with the distribution of thermokarst lakes and known engineering defect points along the Qinghai-Tibet Railway and Highway (Fig. 11a). As thermokarst development and engineering instability are direct manifestations of thawing, this co-location provides robust physical validation for the degradation areas identified by our model. Comparing the environmental variables between the degraded areas and the adjacent stable permafrost reveals that air temperature warming alone does not explain the divergence (Fig. 12). While both regions experienced similar atmospheric warming (mean increase of 0.24 °C in degraded areas versus 0.32 °C in stable areas), the ground thermal response differed significantly (Fig. 12a). The ratio of thawing to freezing indices (*DDT*/*DDF*) increased by 0.22 in the degraded zones, more than double the increase observed in the stable zones (0.10) (Fig. 12b). This amplified thermal forcing was compounded by local surface changes: the soil parameter *E* increased significantly in the degraded areas (+0.079) compared to the stable areas (+0.005) (Fig. 12c). The combination of intensified net heat intake and shifting soil properties pushed the already marginal MAGT, which was approaching 0 °C in the degraded zones (Fig. 12d), past the freezing point, triggering the phase change to SFG.

https://doi.org/10.5194/egusphere-2026-345
Preprint. Discussion started: 4 March 2026

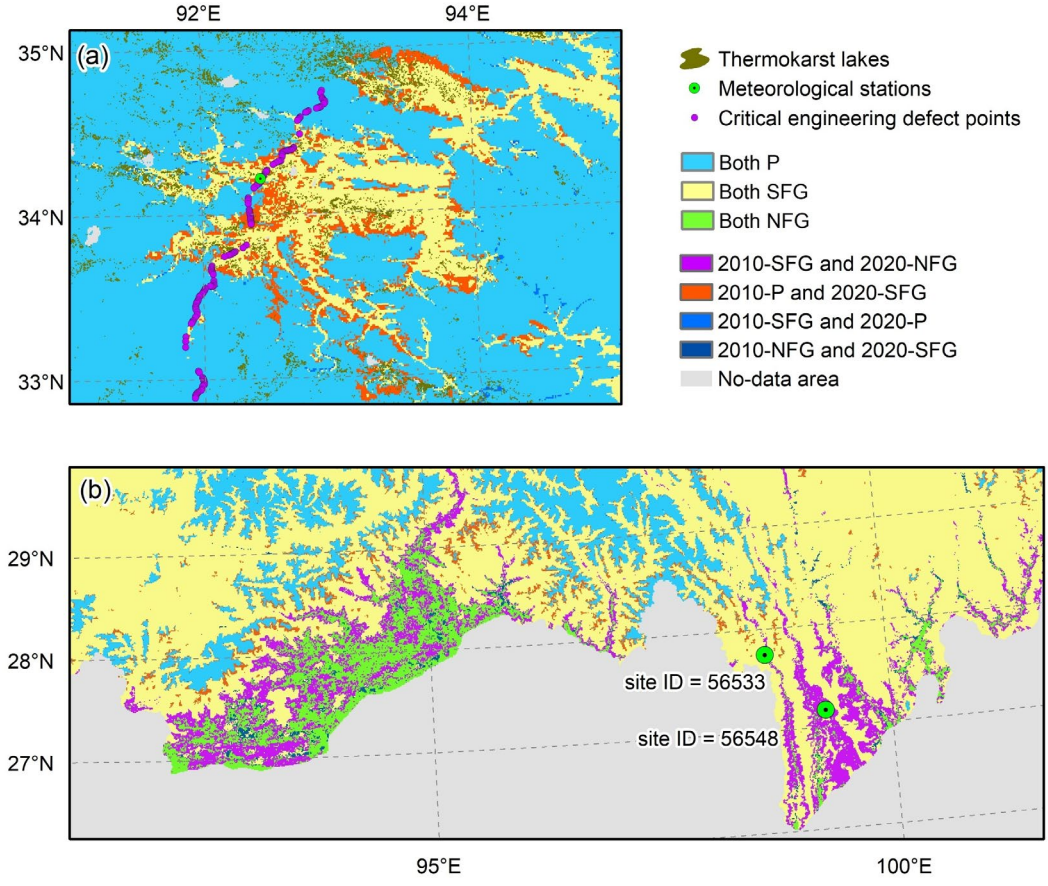

Figure 11 Distribution and changes of frozen ground types in two degradation hotspots on the QTP from 2010 to 2020. Panels (a) and (b) corresponds to subregions (a) and (b) in Fig. 10, respectively. (a) Changes in the central QTP, where the dominant transition is from permafrost to SFG. This map also shows the widespread presence of thermokarst lakes and engineering defect points, serving as proxies for permafrost instability. (b) Changes in the southern QTP, characterized by the transition from SFG to non-frozen ground. The observed 0cm GST values from two meteorological stations (ID: 56533, 56548) provide validation for the model results.

https://doi.org/10.5194/egusphere-2026-345
Preprint. Discussion started: 4 March 2026

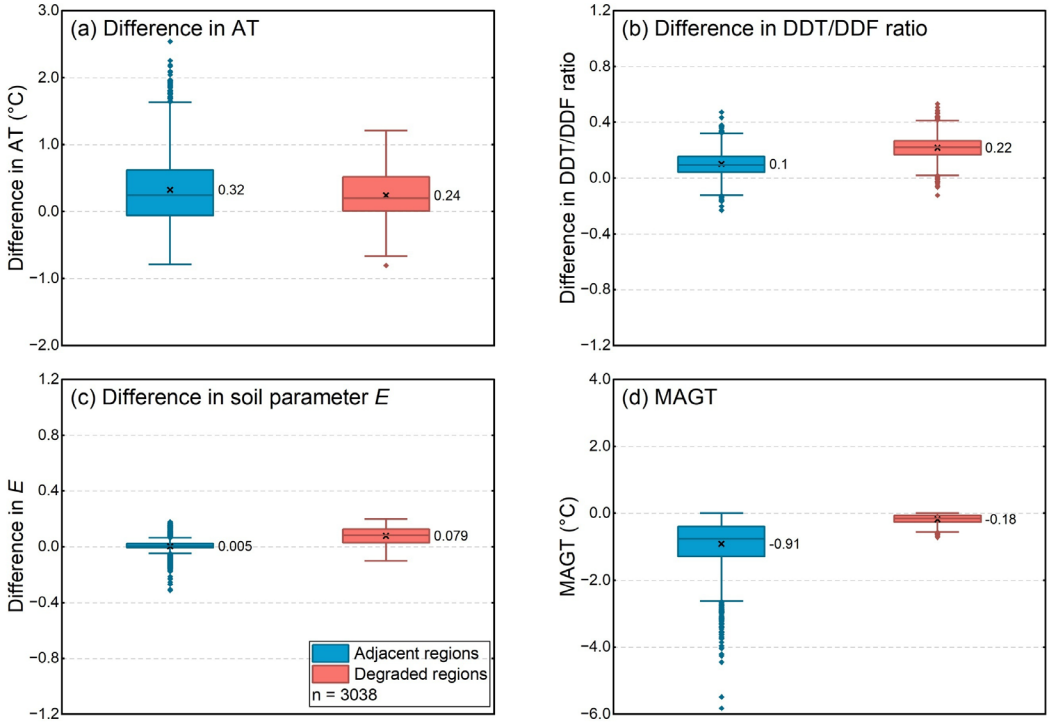

485 **Figure 12 Comparison of key environmental variables between degraded regions (permafrost to SFG) and adjacent stable permafrost regions in subregion a of Fig. 10b (Central QTP). The boxplots compare decadal changes (2010-2020) in (a) air temperature (AT), (b) the *DDT*/*DDF* ratio, and (c) the soil parameter *E*. For the changes shown in panels (a-c), positive values indicate an increase over the decade, while negative values indicate a decrease. Panel (d) compares the mean annual ground temperature (MAGT) in 2010-2019. In each box plot, the center line shows the median, the 'x' marks the mean, the box represents**
490 **the lower and upper quartiles (25th-75th percentiles), and the whiskers extend to the furthest data points within 1.5 times the interquartile range. Data points beyond the whiskers are plotted individually as outliers.**

In contrast, the degradation pattern in the southern QTP (Fig. 11b) was characterized by the contraction of the frozen ground range, manifested as the conversion of SFG to non-frozen ground. Ground-truth validation from meteorological stations 56533 and 56548 confirms this transition: observed records from 2016 to 2019 show a freezing index of zero, indicating the
495 complete absence of ground freezing throughout the year. Mechanism analysis highlights the dominant role of summer warming in this region (Fig. 13). Unlike the central plateau, where *DDF* changes were influential, the southern margin saw the mean *DDT* increase by 310.03 $°C \cdot d$ in degraded areas, compared to only 131.93 $°C \cdot d$ in adjacent SFG regions (Fig. 13b). The *DDF* change was negligible because the *DDF* in these marginal zones was already minimal in 2010 (Fig. 13c). Furthermore, the increase in the local parameter *E* was significantly higher in the degraded region (Fig. 13d). This suggests
500 that the loss of frozen ground here is driven by a massive increase in summer heat input combined with land surface feedbacks that effectively eliminated the shallow seasonal frost layer.

https://doi.org/10.5194/egusphere-2026-345
Preprint. Discussion started: 4 March 2026

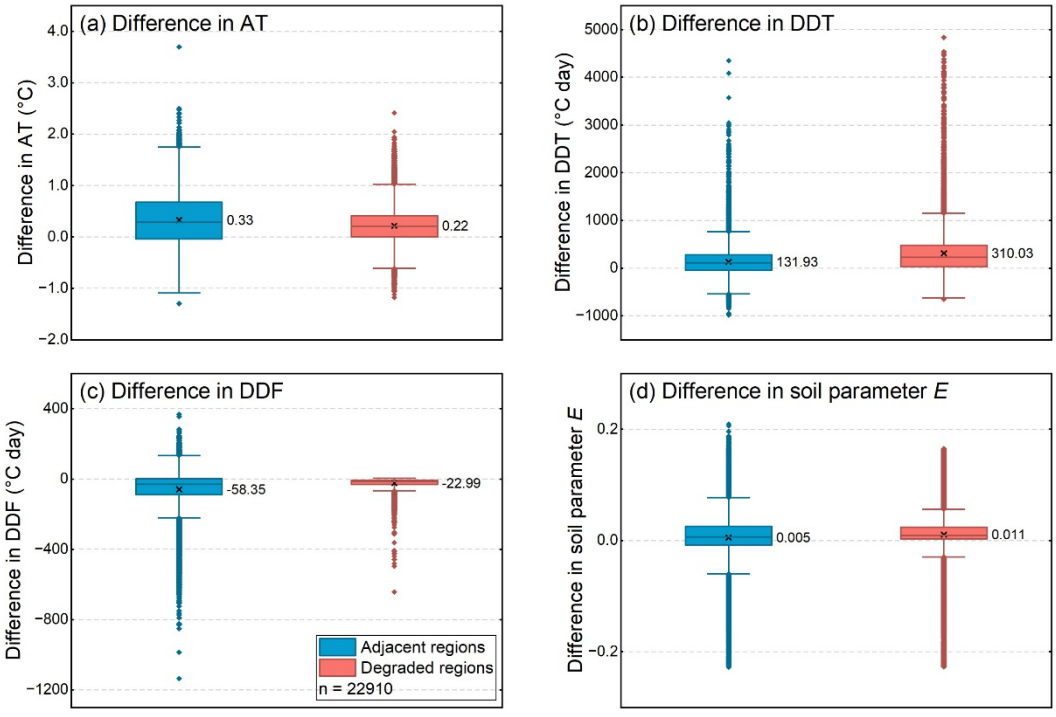

Figure 13 Comparison of key environmental variables between degraded regions (SFG to non-frozen ground) and adjacent SFG regions in subregion b of Fig. 10b (Southern QTP). The panels compare decadal changes in (a) air temperature (AT), (b) *DDT*, (c) *DDF*, and (d) the soil parameter *E*. Positive values indicate an increase over the decade, while negative values indicate a decrease. In each box plot, the centre line shows the median, the 'x' marks the mean, the box represents the lower and upper quartiles (25th-75th percentiles), and whiskers extend to the furthest data points within 1.5 times the interquartile range. Data points beyond the whiskers are plotted individually as outliers.

5 Discussion

The 2020 permafrost distribution map generated in this study demonstrates significant practical value for engineering risk assessment and ecological monitoring on the QTP. The spatial patterns of degradation identified show a high spatial correspondence with known engineering defect points along the Qinghai-Tibet Railway and Highway. This alignment suggests that the map successfully captures the subsurface thermal instability driving infrastructure damage, providing engineers with a critical tool for identifying high-risk zones that require reinforced monitoring. The lowering of the permafrost table in these headwater regions fundamentally alters soil hydrology and vegetation dynamics, offering vital data for assessing the resilience of the Asian Water Tower under continued warming. Beyond its practical applications, this map fills a critical data gap in cryospheric modeling. Unlike previous mapping efforts that often aggregated multi-decadal data to produce climatological averages, this study provides an instantaneous snapshot that captures the frozen ground status at a specific point in time. By offering a temporally specific 2020 benchmark, this dataset enables more rigorous calibration of hydrological and ecological models, ensuring that simulations reflect the current, rather than historical, thermal state of the plateau.

https://doi.org/10.5194/egusphere-2026-345
Preprint. Discussion started: 4 March 2026

In this study, we overcame the lack of concurrent field surveys for 2020. We implemented a space-for-time substitution strategy, hypothesizing that the statistical relationships between the soil parameter and environmental covariates observed in 2010 remained valid for predicting the 2020 state. The comparative evaluation of transfer learning strategies revealed a fundamental trade-off between model complexity and predictive stability. While the hybrid neural network (MLP) theoretically offered greater flexibility, it exhibited severe overfitting and generated implausible spatial artifacts when applied to the plateau-wide domain. In contrast, the RF-based strategy demonstrated superior robustness. By treating the problem as a regression of the 16-class *E*-field, the RF algorithm effectively filtered noise and captured the large-scale zonal patterns of soil properties, making it the more suitable choice for this specific application.

However, the methodology remains subject to certain limitations. The space-for-time substitution relies on the premise that the interaction between environmental drivers and ground thermal properties is stationary over the study period. While this assumption is reasonable for a decadal timescale, it introduces uncertainty when applied over longer periods or under abruptly changing environmental conditions where the equilibrium between climate and soil properties might decouple. Furthermore, the lack of updated large-scale field surveys means that the 2020 *E* parameter remains a modeled estimate rather than a calibrated observation.

Looking forward, these limitations point to clear directions for methodological advancement. Future research should prioritize the acquisition of updated field survey data to provide direct constraints on parameter estimation. Additionally, the potential of neural network approaches should not be dismissed based on the failure of the unconstrained MLP. The overfitting issues observed here could likely be mitigated by embedding physical constraints directly into the loss function. The development of such physics-constrained learning frameworks represents a promising avenue for achieving continuous, high-resolution parameter estimation while maintaining the physical realism required for reliable cryospheric modeling.

6 Data availability

The dataset generated in this study, comprising the 1-km resolution permafrost distribution of the QTP for 2020 and the associated annual ground surface freezing and thawing indices derived from MODIS data is publicly available via Figshare (Chen et al., 2026): https://doi.org/10.6084/m9.figshare.30997375. The sources and access details for the third-party public datasets utilized for model forcing and validation are listed in Appendix C.

7 Conclusions

This study produced a 1-km resolution permafrost distribution map for the QTP for the year 2020 by advancing the ground surface frost number model (FROSTNUM) framework. To address the challenge of data scarcity in updating the 2020 map, we implemented a space-for-time substitution strategy to estimate the critical soil parameter *E*. Our comparative evaluation demonstrated that a RF regression approach, trained on representative spatial samples in the 2010 map, provided a robust and

https://doi.org/10.5194/egusphere-2026-345
Preprint. Discussion started: 4 March 2026

physically realistic estimation of soil parameters, whereas unconstrained neural network (MLP) approach suffered from overfitting and spatial artifacts.

The resulting 2020 map reveals that permafrost covers approximately 1.038×10^6 km² (39.35% of the total QTP area), while SFG covers 1.466×10^6 km² (55.57%). Validation against 109 independent borehole records, the map achieved an overall accuracy of 0.84 and a Cohen's Kappa of 0.58, demonstrating superior performance compared to existing MAGT-based and TTOP-based products.

A systematic comparison with the 2010 baseline indicates a significant degradation of the frozen ground extent over the decade. The total permafrost area decreased by 4.8×10^4 km² (a 1.82% decrease), primarily transitioned into SFG. Spatially, this degradation was concentrated in two distinct hotspots driven by rising ground temperatures. In the central QTP, widespread degradation of unstable permafrost accounted for 7.41% of the total changes. Conversely, the southern margins experienced a rapid contraction of the frozen ground range, where the conversion of SFG to non-frozen ground accounted for 39.62% of the total changes.

This study provided a critical, up-to-date benchmark of the QTP's frozen ground status. The produced map serves as a vital resource for engineering risk assessment, ecological monitoring, and the rigorous calibration of land surface models in this rapidly warming QTP.

Appendix A: Sampling strategies for optimization of the Random Forest training set

We implemented a representative sampling framework for training the RF model efficiently while capturing the full heterogeneity of the QTP. The primary objective was to select a subset of training pixels from the comprehensive dataset (exceeding 2 million grid cells) that minimized information redundancy while maximizing the environmental variance covered by the model. This is critical for reducing predictive uncertainty, particularly for rare but physically significant permafrost conditions. We evaluated four distinct sampling algorithms: *k*-means clustering sampling (Brus et al., 2006), the Equal Range (ER) sampling (Hengl et al., 2003), Principal Component Analysis (PCA)-based sampling (Hengl et al., 2003), and Latin Hypercube Sampling (LHS) (Carré et al., 2007) across four sample sizes (1000, 3000, 5000, and 10000 points).

k-means clustering sampling: This method utilizes unsupervised learning to partition the multivariate environmental space into distinct clusters, ensuring that the training set represents distinct physical conditions rather than oversampling spatially abundant but homogeneous areas (Hartigan, 1975). We applied *k*-means algorithm to the vectors of the environmental covariates (topography, soil, vegetation, etc.). The algorithm partitions the study domain into k clusters by minimizing the within-cluster sum of squares. For each cluster, the pixel located closest to the geometric centroids in the feature space was selected as the representative training sample. This approach inherently prioritizes environmental representativeness over spatial proximity.

ER sampling: Standard random sampling often results in a majority class bias, where the model learns the characteristics of common conditions well but fails to predict rare extremes. To mitigate this, we employed ER sampling, which stratifies the

https://doi.org/10.5194/egusphere-2026-345
Preprint. Discussion started: 4 March 2026

sampling domain based on the distribution of key environmental gradients (Hengl et al., 2003). The core principle of ER is to divide the entire range of a predictor variable into several equal-width strata (or histogram slices). Samples are then allocated within these strata proportionally to the data density. For example, considering a variable with a normal distribution divided into 5 clusters across its standard statistical range (-3σ to + 3σ), the stratification limits correspond to cumulative probabilities of 3.6%, 27.4%, 72.6%, 96.4%, and 100%. Consequently, the sampling weights are assigned to these strata are 0.036, 0.238, 0.452, 0.238, and 0.036, respectively. This method remains robust even for skewed distributions. In our implementation, we generated sample allocations for each environmental factor independently, dividing the total target sample size equally among the factors. We then aggregated these individual sample sets into a combined training pool. Finally, a deduplication step was applied to remove any overlapping points. Testing confirmed that this deduplication resulted in a negligible reduction in the final count, thereby preserving the intended sample size.

PCA-based sampling: The environmental covariates driving permafrost distribution often exhibit high multicollinearity. The PCA-based method (Hengl et al., 2003) address this by transforming the original, correlated predictors into a set of principle components. Sampling was then conducted in this reduced PC space to maximize the coverage of environmental variability. In our implementation, we first performed a PCA analysis on all environmental factors and retained the components that cumulatively explained 95% of the total variance. The total sample size was then allocated to these selected PCs in proportion to the variance they explained. For example, given a target of 10,000 samples, if the first PC accounted for 64% of the variance, 6,400 sample points were allocated to it. The selection of specific points was achieved by stratifying each retained PC using the ER method and randomly drawing the allocated number of samples from within those strata.

LHS sampling: LHS is a constrained Monte Carlo scheme widely recognized for its efficiency in sampling when no prior soil samples exist, relying solely on ancillary data (Carré et al., 2007). It is a stratified-random procedure designed to ensure that the full range of every variable is sampled with uniform probability. The method operates by dividing the cumulative distribution of each of the k environmental variables into n equiprobable intervals (where n is the target sample size). A single value is randomly selected from each interval for every variable. Finally, these n values for each variable are randomly paired to create n unique, multivariate sample points. This process ensures that the marginal distribution of each variable is maximally stratified, guaranteeing that the training set covers the entire multivariate feature space without the clustering or gaps common in simple random sampling.

Appendix B: Evaluation of the MLP-derived E values

We conducted an analysis to evaluate the validity of the soil parameter E predicted by the Multi-Layer Perceptron (MLP) model. The evaluation focused on both the statistical distribution of the predicted values and the spatial realism of the resulting permafrost simulation.

As shown in Fig. B1, the MLP-predicted E values exhibit a highly irregular statistical distribution that deviates from physical expectations. Approximately 53% of the total pixels fall within the range of 0-2.0 (Fig. B1a), with the highest

https://doi.org/10.5194/egusphere-2026-345
Preprint. Discussion started: 4 March 2026

615 frequency heavily skewed towards the 0-0.1 interval. Conversely, the remaining 47% of the values are scattered across an unrealistically wide range of 2.0-350 (Fig. B1b). This extreme bifurcation suggests the model failed to learn the continuous physical properties of the soil, instead overfitting to the binary classification targets.

Spatially, the MLP-derived *E* field (Fig. B2a) displays significant inconsistencies when compared to the reference *E* distribution derived from the Particle Swarm Optimization algorithm with boundary constraints (Fig. B2b), which served as 620 the validated baseline in Cao et al. (2023). Due to the absence of physical constraints, the MLP-derived *E* values exhibit extreme spatial heterogeneity and magnitude deviations of several orders.

The practical consequences of these artifacts are evident when the MLP-derived *E* field is used to reconstruct the permafrost distribution for 2010. The resulting map (Fig. B2c) exhibits a substantial visual and spatial mismatch with the rigorously validated 2010 baseline map (Fig. B2d). Given these fundamental discrepancies in both statistical distribution and 625 spatial patterns, we conclude that the unconstrained MLP approach does not accurately reflect actual soil conditions. Consequently, this method was excluded from the final mapping workflow. Future applications of deep learning in this context would likely require the integration of physical constraints or penalty terms to ensure physically realistic parameter estimation.

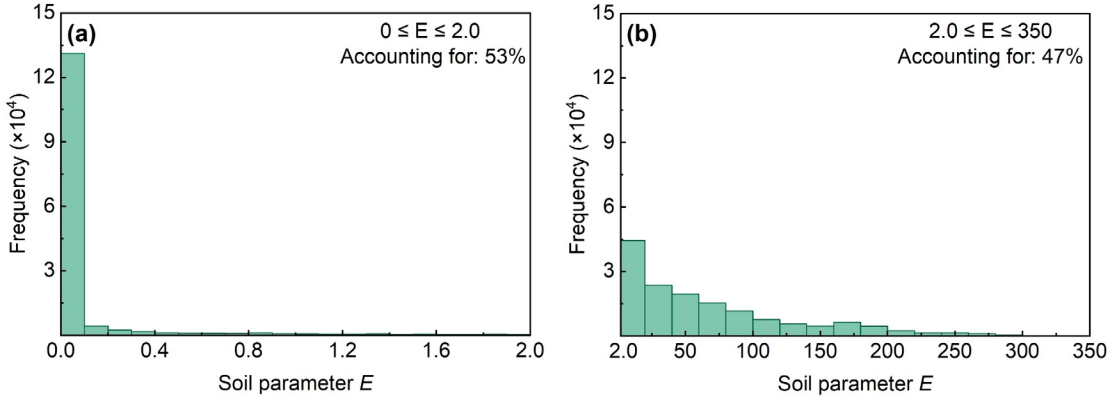

Figure B1. Frequency histograms of the soil parameter *E* predicted by the MLP model. (a) Distribution of values within the 630 range of $0 \leq E \leq 2.0$, accounting for 53% of total pixels. (b) Distribution of values within the range of $2.0 \leq E \leq 350$, accounting for the remaining 47%.

https://doi.org/10.5194/egusphere-2026-345
Preprint. Discussion started: 4 March 2026

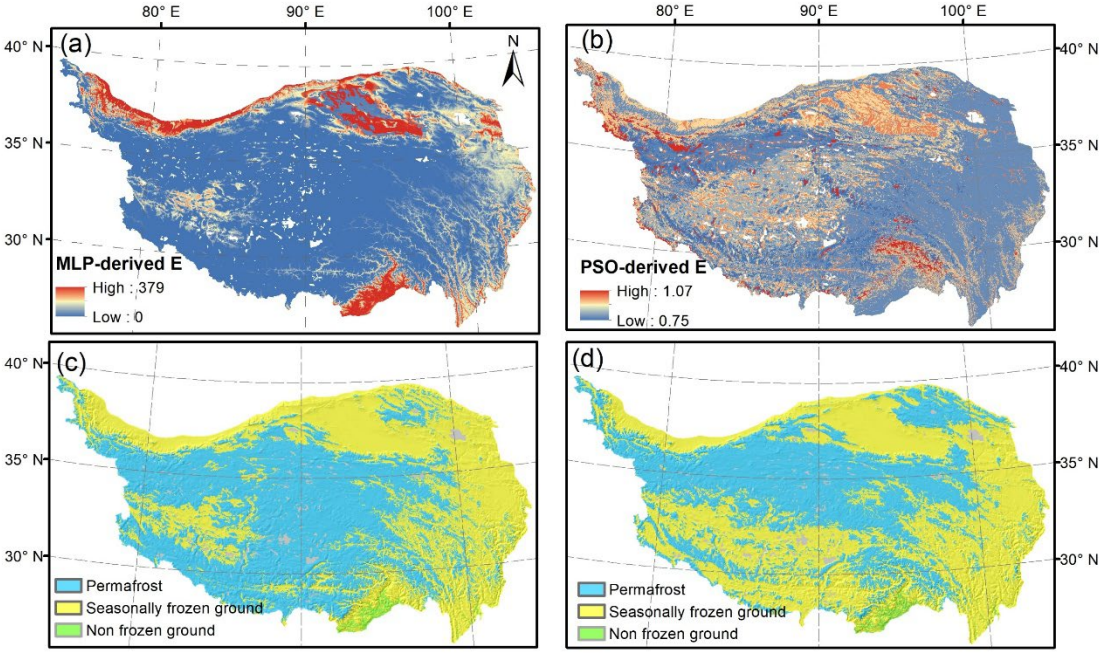

Figure B2. Comparison of the spatial distribution of soil parameter *E* and the resulting frozen ground types. (a) Spatial distribution of *E* derived from the MLP model. (b) Spatial distribution of *E* derived from the Particle Swarm Optimization algorithm (Cao et al., 2023). (c) Frozen ground distribution simulated using the MLP-derived *E*. (d) Validated baseline frozen ground map for the year 2010.

Appendix C: Sources of open datasets used

This study utilized several publicly available datasets. The daily MODIS LST and emissivity products (MOD11A1 and MYD11A1 version 6) (https://doi.org/10.5067/MODIS/MOD11A1.006, https://doi.org/10.5067/MODIS/MYD11A1.006) and the NDVI product (MOD13A1) (https://doi.org/10.5067/MODIS/MOD13A1.006) are provided by NASA. Topographic data was sourced from the SRTM 90m DEM (version 4; (Reuter et al., 2007)) (https://cgiarcsi.community/data/srtm-90m-digital-elevation-database-v4-1/, accessed on January 6, 2026). Climatic data and surface data: the 1 km monthly precipitation dataset for China (Peng et al., 2019) (https://doi.org/10.5281/zenodo.3185722); the 0.005° daily Fractional Snow Cover Dataset Over High Asia (Pan et al., 2024) (https://doi.org/10.11888/Cryos.tpdc.272503); and soil properties from the China Data Set of Soil Properties for Land Surface modeling (Shangguan et al., 2013) (http://globalchange.bnu.edu.cn/research/soil2, accessed on January 6, 2026). Ground-truth and comparison datasets included: the Daily Meteorological Dataset of Basic Meteorological Elements of China National Surface Weather Station (1991-2020) from China National Meteorological Information Centre (Zhao et al., 2024; available upon registration and request at https://data.cma.cn/ due to the data provider's licensing policies); borehole ground temperature data from Zhao et al. (2021) (https://doi.org/10.11888/Geocry.tpdc.271107); a permafrost

https://doi.org/10.5194/egusphere-2026-345
Preprint. Discussion started: 4 March 2026

distribution map based on the Top of Permafrost (TTOP) from Yan et al. (2023)(https://doi.org/10.11888/Cryos.tpdc.300955); and ground temperature data at 15 m depth for 2010-2019 from Zou et al. (2025) (https://doi.org/10.11888/Cryos.tpdc.301165). Our 2020 permafrost distribution map and associated data are available at Figshare (Chen et al., 2026): https://doi.org/10.6084/m9.figshare.30997375.

Author contributions

Conceptualization, Z.N.; Methodology, Z.N. and Y.C.; Formal analysis, Y.C., W.T. and Y.Z.; Validation, Y.C. and Y.Z.; Writing—original draft, Y.C. and Z.N.; Writing—review and editing, Z.N., Y.C., S.Z., D.Y., G.J. and F.N.; Supervision, Z.N.; Funding acquisition, Z.N. and Y.C.. All authors have read and agree to the published version of the manuscript.

Competing interests

The contact author has declared that none of the authors has any competing interests.

Acknowledgements

The authors gratefully acknowledge the National Tibetan Plateau Data Center and NASA for providing the datasets used in this study. Sincere appreciation is also extended to the scientists who participated in the Second Tibetan Plateau Scientific Expedition and Research campaign for their dedicated efforts in collecting valuable in situ data across the Qinghai-Tibet Plateau.

Financial support

This research was supported by the grant of National Natural Science Foundation of China (No. 42571149). Yuhong Chen was also supported by the Postdoctoral Research Funding of Hangzhou International Innovation Institute of Beihang University (Grant No. 2025BKZ075).

https://doi.org/10.5194/egusphere-2026-345
Preprint. Discussion started: 4 March 2026

References

Brus, D. J., de Gruijter, J. J., and van Groenigen, J. W.: Chapter 14 Designing spatial coverage samples using the k-means clustering algorithm, in: Developments in Soil Science, edited by: P. Lagacherie, A.B McBratney, and M. Voltz, Elsevier, Amsterdam, Netherlands, 183-192, https://doi.org/10.1016/S0166-2481(06)31014-8, 2006.

Burke, E. J., Zhang, Y., and Krinner, G.: Evaluating permafrost physics in the Coupled Model Intercomparison Project 6 (CMIP6) models and their sensitivity to climate change, The Cryosphere, 14, 3155-3174, https://doi.org/10.5194/tc-14-3155-2020, 2020.

Cao, Z., Nan, Z., Hu, J., Chen, Y., and Zhang, Y.: A new 2010 permafrost distribution map over the Qinghai–Tibet Plateau based on subregion survey maps: a benchmark for regional permafrost modeling, Earth Syst. Sci. Data, 15, 3905-3930, https://doi.org/10.5194/essd-15-3905-2023, 2023.

Carré, F., Mcbratney, A. B., and Minasny, B.: Estimation and potential improvement of the quality of legacy soil samples for digital soil mapping, Geoderma, 141, 1-14, https://doi.org/10.1016/j.geoderma.2007.01.018, 2007.

Chadburn, S. E., Burke, E. J., Cox, P. M., Friedlingstein, P., Hugelius, G., and Westermann, S.: An observation-based constraint on permafrost loss as a function of global warming, Nat. Clim. Chang., 7, 340-344, https://doi.org/10.1038/nclimate3262, 2017.

Chen, Y., Nan, Z., Cao, Z., Ou, M., and Feng, K.: A stepwise framework for interpolating land surface temperature under cloudy conditions based on the solar-cloud-satellite geometry, ISPRS-J. Photogramm. Remote Sens., 197, 292-308, https://doi.org/10.1016/j.isprsjprs.2023.02.004, 2023.

Chen, Y., Nan, Z., Tian, W., Zhao, Y., Zhao, S., Yang, D., Jing, G., and Niu, F.: A 2020 permafrost distribution map over the Qinghai-Tibet Plateau, Figshare [data set], https://doi.org/10.6084/m9.figshare.30997375, 2026.

Cheng, G., Li, S., and Nan, Z.: Map of permafrost on the Qinghai-Tibet Plateau (1:3,000,000) (1983-1996), National Tibetan Plateau Data Center [data set], https://doi.org/10.11888/Geocry.tpdc.270014, 1996.

Deng, H., Zhang, Z., and Wu, Y.: Accelerated permafrost degradation in thermokarst landforms in Qilian Mountains from 2007 to 2020 observed by SBAS-InSAR, Ecol. Indic., 159, 111724, https://doi.org/10.1016/j.ecolind.2024.111724, 2024.

Fu, Y., Horton, R., and Heitman, J.: Neural network estimation of thermal conductivity across full saturation for various soil types, Comput. Electron. Agric., 235, 110321, https://doi.org/10.1016/j.compag.2025.110321, 2025.

Gay, B. A., Pastick, N. J., Züfle, A. E., Armstrong, A. H., Miner, K. R., and Qu, J. J.: Investigating permafrost carbon dynamics in Alaska with artificial intelligence, Environ. Res. Lett., 18, 125001, https://doi.org/10.1088/1748-9326/ad0607, 2023.

Guo, D. and Wang, H.: Simulation of permafrost and seasonally frozen ground conditions on the Tibetan Plateau, 1981–2010, J. Geophys. Res.-Atmos., 118, 5216-5230, https://doi.org/10.1002/jgrd.50457, 2013.

Hachem, S., Allard, M., and Duguay, C.: Using the MODIS land surface temperature product for mapping permafrost: an application to northern Québec and Labrador, Canada, Permafrost and Periglacial Processes, 20, 407-416, https://doi.org/10.1002/ppp.672, 2009.

https://doi.org/10.5194/egusphere-2026-345
Preprint. Discussion started: 4 March 2026

Hartigan, J.: Clustering algorithms, Wiley, New York, USA, 364 pp., ISBN 0-471-35645-X, 1975.

Hengl, T., Rossiter, D. G., and Stein, A. G.: Soil sampling strategies for spatial prediction by correlation with auxiliary maps, Australian Journal of Soil Research, 41, 1403-1422, https://doi.org/10.1071/SR03005, 2003.

Hjort, J., Streletskiy, D., Doré, G., Wu, Q., Bjella, K., and Luoto, M.: Impacts of permafrost degradation on infrastructure, Nat. Rev. Earth Environ., 3, 24-38, https://doi.org/10.1038/s43017-021-00247-8, 2022.

Hu, G., Zhao, L., Sun, Z., Zou, D., Xiao, Y., Liu, G., Du, E., Wang, C., Wang, Y., Wu, X., Wang, L., and Zhao, Y.: Spatiotemporal characteristics and variability in the thermal state of permafrost on the Qinghai-Tibet Plateau, Permafrost and Periglacial Processes, 35, 143-156, https://doi.org/10.1002/ppp.2219, 2024.

Hu, G., Zhao, L., Wu, X., Li, R., Wu, T., Su, Y., and Hao, J.: Evaluation of reanalysis air temperature products in permafrost regions on the Qinghai-Tibetan Plateau, Theor. Appl. Climatol., 138, 1457-1470, https://doi.org/10.1007/s00704-019-02888-8, 2019.

Hu, J., Zhao, S., Nan, Z., Wu, X., Sun, X., and Cheng, G.: An effective approach for mapping permafrost in a large area using subregion maps and satellite data, Permafrost and Periglacial Processes, 31, 548-560, https://doi.org/10.1002/ppp.2068, 2020.

Huang, X., Tang, G., Zhu, T., Ding, H., and Na, J.: Space-for-time substitution in geomorphology: A critical review and conceptual framework, J. Geogr. Sci., 29, 1670-1680, https://doi.org/10.1007/s11442-019-1684-0, 2019.

Jia, Y., Chen, S., Wu, M., Gu, Y., Wei, P., Wu, T., Shang, Z., Wang, S., and Yu, H.: Improved permafrost stability by revegetation in extremely degraded grassland of the Qinghai-Tibetan Plateau, Geoderma, 430, 116350, https://doi.org/10.1016/j.geoderma.2023.116350, 2023.

Karjalainen, O., Luoto, M., Aalto, J., and Hjort, J.: New insights into the environmental factors controlling the ground thermal regime across the Northern Hemisphere: a comparison between permafrost and non-permafrost areas, The Cryosphere, 13, 693-707, https://doi.org/10.5194/tc-13-693-2019, 2019.

Kim, K. Y., Haagenson, R., Kansara, P., Rajaram, H., and Lakshmi, V.: Augmenting daily MODIS LST with AIRS surface temperature retrievals to estimate ground temperature and permafrost extent in High Mountain Asia, Remote Sens. Environ., 305, 114075, https://doi.org/10.1016/j.rse.2024.114075, 2024.

Kukulies, J., Chen, D., and Wang, M.: Temporal and spatial variations of convection, clouds and precipitation over the Tibetan Plateau from recent satellite observations. Part II: Precipitation climatology derived from global precipitation measurement mission, Int. J. Climatol., 40, 4858-4875, https://doi.org/10.1002/joc.6493, 2020.

Lei, W., Luo, D., Chen, F., Liu, J., Peng, Y., Li, S., and Shen, Q.: Changes in the thermal regime of permafrost in the Headwater Area of the Yellow River in 1979-2018 based on the HYDRUS model, Advances in Earth Science, 39, 1-13, https://doi.org/10.11867/j. issn.1001-8166.2024.084, 2024 (in Chinese).

Lewkowicz, A. G., O'Neill, H. B., Wolfe, S. A., Roy-Léveillée, P., Roujanski, V. E., Hoever, E., Gruber, S., Brooks, H., Rudy, A. C., Koenig, C. E. M., Brown, N., and Bonnaventure, P. P.: Glossary of Permafrost Science and Engineering, Canadian Permafrost Association, Toronto, Canada, 188 pp., http://doi.org/10.3138/cpa-gpse, 2025.

https://doi.org/10.5194/egusphere-2026-345
Preprint. Discussion started: 4 March 2026

Li, X. and Cheng, G.: A GIS-aided response model of high-altitude permafrost to global change, Science in China Series D: Earth Sciences, 42, 72-79, https://doi.org/10.1007/BF02878500, 1999.

Li, X., Cheng, G., Jin, H., Kang, E., Che, T., Jin, R., Wu, L., Nan, Z., Wang, J., and Shen, Y.: Cryospheric change in China, Glob. Planet. Change, 62, 210-218, https://doi.org/10.1016/j.gloplacha.2008.02.001, 2008.

Li, Z., Zhao, L., Liu, G., Zou, D., Wang, L., Yang, B., Du, E., Hu, G., Zhou, H., and Wang, C.: Analysis of soil moisture content in the active layer in the permafrost region of the Tuotuo River source in frozen season, Journal of Glaciology and Geocryology, 44, 56-68, https://doi.org/10.7522/j.issn.1000-0240.2022.0001, 2022.

Mao, J., Shi, X., Ma, L., Kaiser, D. P., Li, Q., and Thornton, P. E.: Assessment of reanalysis daily extreme temperatures with China's homogenized historical dataset during 1979–2001 using probability density functions, J. Clim., 23, 6605-6623, https://doi.org/10.1175/2010JCLI3581.1, 2010.

Mi, D.: Map of snow, ice and frozen ground in China, Journal of Glaciology and Geocryology, 12, 175-181, https://doi.org/10.7522/j.issn.1000-0240.1990.0054, 1990.

Mu, C., Abbott, B. W., Norris, A. J., Mu, M., Fan, C., Chen, X., Jia, L., Yang, R., Zhang, T., Wang, K., Peng, X., Wu, Q., Guggenberger, G., and Wu, X.: The status and stability of permafrost carbon on the Tibetan Plateau, Earth-Sci. Rev., 211, 103433, https://doi.org/10.1016/j.earscirev.2020.103433, 2020.

Mu, C., Peng, X., Du, R., Liu, H., Jin, H., Liang, B., Mu, M., Sun, W., Fan, C., Wu, X., Frauenfeld, O. W., and Zhang, T.: A comprehensive dataset for earth system models in a permafrost region: meteorological, permafrost, and carbon observations (2011–2020) in Northeastern Qinghai-Tibet Plateau, Earth System Science Data Discussions, 2022, 1-32, https://doi.org/10.5194/essd-2022-347, 2022.

Nan, Z., Huang, P., and Zhao, L.: Permafrost distribution modeling and depth estimation in the Western Qinghai-Tibet Plateau, Acta Geographica Sinica, 68, 318-327, https://doi.org/10.11821/xb201303003, 2013 (in Chinese).

Nan, Z., Li, S., and Liu, Y.: Mean annual ground temperature distribution on the Tibetan Plateau: permafrost distribution mapping and further application, Journal of Glaciology and Geocryology, 24, 142-148, https://doi.org/10.7522/j.issn.1000-0240.2002.0024, 2002.

Ni, J., Du, Y., Wu, T., Mo, Q., Zhang, X., and Su, Y.: Hydrothermal variations of active layer in permafrost regions and the influence of vegetation in the Qinghai-Tibetan Plateau, Theor. Appl. Climatol., 156, 12, https://doi.org/10.1007/s00704-024-05286-x, 2025.

Ni, J., Wu, T., Zhu, X., Hu, G., Zou, D., Wu, X., Li, R., Xie, C., Qiao, Y., Pang, Q., Hao, J., and Yang, C.: Simulation of the present and future projection of permafrost on the Qinghai-Tibet Plateau with statistical and machine learning models, J. Geophys. Res.-Atmos., 126, e2020JD033402, https://doi.org/10.1029/2020JD033402, 2021.

Obu, J., Westermann, S., Bartsch, A., Berdnikov, N., Christiansen, H. H., Dashtseren, A., Delaloye, R., Elberling, B., Etzelmüller, B., Kholodov, A., Khomutov, A., Kääb, A., Leibman, M. O., Lewkowicz, A. G., Panda, S. K., Romanovsky, V., Way, R. G., Westergaard-Nielsen, A., Wu, T., Yamkhin, J., and Zou, D.: Northern Hemisphere permafrost map based on TTOP modelling for 2000–2016 at 1 km^2 scale, Earth-Sci. Rev., 193, 299-316,

https://doi.org/10.1016/j.earscirev.2019.04.023, 2019.

Pan, F., Jiang, L., Wang, G., Pan, J., Huang, J., Zhang, C., Cui, H., Yang, J., Zheng, Z., Wu, S., and Shi, J.: MODIS daily cloud-gap-filled fractional snow cover dataset of the Asian Water Tower region (2000–2022), Earth Syst. Sci. Data, 16, 2501-2523, https://doi.org/10.5194/essd-16-2501-2024, 2024.

Pan, Y., Li, X., and Li, S.: Effects of different soil thermal conductivity schemes on the simulation of permafrost on the Tibetan Plateau, Geoderma, 442, 116789, https://doi.org/10.1016/j.geoderma.2024.116789, 2024.

Park, Y. and Lek, S.: Chapter 7 - Artificial neural networks: Multilayer perceptron for ecological modeling, in: Developments in Environmental Modelling, edited by: Sven Erik Jørgensen, Elsevier, Amsterdam, Netherlands, 123-140, https://doi.org/10.1016/B978-0-444-63623-2.00007-4, 2016.

Peng, S., Ding, Y., Liu, W., and Li, Z.: 1 km monthly temperature and precipitation dataset for China from 1901 to 2017, Earth Syst. Sci. Data, 11, 1931-1946, https://doi.org/10.5194/essd-11-1931-2019, 2019.

Pickett, S. T.: Space-for-time substitution as an alternative to long-term studies, in: Long-Term Studies in Ecology, edited by: Gene E. Likens, Springer, New York, USA, 110-135, https://doi.org/10.1007/978-1-4615-7358-6_5, 1989.

Qiu, J.: China: The third pole, Nature, 454, 393-396, https://doi.org/10.1038/454393a, 2008.

Ran, Y., Li, X., Cheng, G., Che, J., Aalto, J., Karjalainen, O., Hjort, J., Luoto, M., Jin, H., Obu, J., Hori, M., Yu, Q., and Chang, X.: New high-resolution estimates of the permafrost thermal state and hydrothermal conditions over the Northern Hemisphere, Earth Syst. Sci. Data, 14, 865-884, https://doi.org/10.5194/essd-14-865-2022, 2022.

Reuter, H. I., Nelson, A., and Jarvis, A.: An evaluation of void-filling interpolation methods for SRTM data, Geogr. Inf. Syst., 21, 983-1008, https://doi.org/10.1080/13658810601169899, 2007.

Shan, W., Zhang, C., Guo, Y., and Qiu, L.: Mapping the thermal state of permafrost in Northeast China based on the surface frost number model, Remote Sens., 14, 3185, https://doi.org/10.3390/rs14133185, 2022.

Shangguan, W., Dai, Y., Liu, B., Zhu, A., Duan, Q., Wu, L., Ji, D., Ye, A., Yuan, H., Zhang, Q., Chen, D., Chen, M., Chu, J., Dou, Y., Guo, J., Li, H., Li, J., Liang, L., Liang, X., Liu, H., Liu, S., Miao, C., and Zhang, Y.: A China data set of soil properties for land surface modeling, J. Adv. Model. Earth Syst., 5, 212-224, https://doi.org/10.1002/jame.20026, 2013.

Shi, S., Wang, P., Zhan, X., Han, J., Guo, M., and Wang, F.: Warming and increasing precipitation induced greening on the northern Qinghai-Tibet Plateau, Catena, 233, 107483, https://doi.org/10.1016/j.catena.2023.107483, 2023.

Siewert, M. B.: High-resolution digital mapping of soil organic carbon in permafrost terrain using machine learning: a case study in a sub-Arctic peatland environment, Biogeosciences, 15, 1663-1682, https://doi.org/10.5194/bg-15-1663-2018, 2018.

Smith, M. W. and Riseborough, D. W.: Permafrost monitoring and detection of climate change, Permafrost and Periglacial Processes, 7, 301-309, https://doi.org/10.1002/(SICI)1099-1530(199610)7:4<301::AID-PPP231>3.0.CO;2-R, 1996.

Smith, S. L., O'Neill, H. B., Isaksen, K., Noetzli, J., Romanovsky, V. E., and Anonymous: The changing thermal state of permafrost, Nat. Rev. Earth Environ., 3, 10-23, https://doi.org/10.1038/s43017-021-00240-1, 2022.

Tananaev, N. and Lotsari, E.: Defrosting northern catchments: Fluvial effects of permafrost degradation, Earth-Sci. Rev., 228,

https://doi.org/10.5194/egusphere-2026-345
Preprint. Discussion started: 4 March 2026

103996, https://doi.org/10.1016/j.earscirev.2022.103996, 2022.

van Der Westhuizen, S., Heuvelink, G. B., and Hofmeyr, D. P.: Multivariate random forest for digital soil mapping, Geoderma, 431, 116365, https://doi.org/10.1016/j.geoderma.2023.116365, 2023.

van Doninck, J., Peters, J., De Baets, B., De Clercq, E. M., Ducheyne, E., and Verhoest, N. E. C.: The potential of multitemporal Aqua and Terra MODIS apparent thermal inertia as a soil moisture indicator, Int. J. Appl. Earth Obs. Geoinf., 13, 934-941, https://doi.org/10.1016/j.jag.2011.07.003, 2011.

Wadoux, A. M., Brus, D. J., and Heuvelink, G. B.: Sampling design optimization for soil mapping with random forest, Geoderma, 355, 113913, https://doi.org/10.1016/j.geoderma.2019.113913, 2019.

Wang, G., Liu, G., Li, C., and Yang, Y.: The variability of soil thermal and hydrological dynamics with vegetation cover in a permafrost region, Agric. For. Meteorol., 162-163, 44-57, https://doi.org/10.1016/j.agrformet.2012.04.006, 2012.

Wang, Y., Lv, W., Xue, K., Wang, S., Zhang, L., Hu, R., Zeng, H., Xu, X., Li, Y., and Jiang, L.: Grassland changes and adaptive management on the Qinghai–Tibetan Plateau, Nat. Rev. Earth Environ., 3, 668-683, https://doi.org/10.1038/s43017-022-00330-8, 2022.

Wu, Q. and Zhang, T.: Recent permafrost warming on the Qinghai-Tibetan Plateau, Journal of Geophysical Research: Atmospheres, 113, https://doi.org/10.1029/2007JD009539, 2008.

Yan, D., Zheng, X., Feng, M., Liang, S., Hu, Z., Kuang, X., and Feng, Y.: Frozen ground change data set in the Tibetan Plateau (1961-2020), National Tibetan Plateau/Third Pole Environment Data Center [data set], https://doi.org/10.11888/Cryos.tpdc.300955, 2023.

Yang, M., Nelson, F. E., Shiklomanov, N. I., Guo, D., and Wan, G.: Permafrost degradation and its environmental effects on the Tibetan Plateau: A review of recent research, Earth-Sci. Rev., 103, 31-44, https://doi.org/10.1016/j.earscirev.2010.07.002, 2010.

Yang, M., Wang, X., Pang, G., Wan, G., and Liu, Z.: The Tibetan Plateau cryosphere: Observations and model simulations for current status and recent changes, Earth-Sci. Rev., 190, 353-369, https://doi.org/10.1016/j.earscirev.2018.12.018, 2019.

Yao, T., Bolch, T., Chen, D., Gao, J., Immerzeel, W., Piao, S., Su, F., Thompson, L., Wada, Y., and Wang, L.: The imbalance of the Asian water tower, Nat. Rev. Earth Environ., 3, 618-632, https://doi.org/10.1038/s43017-022-00299-4, 2022.

Yao, T., Thompson, L., Yang, W., Yu, W., Gao, Y., Guo, X., Yang, X., Duan, K., Zhao, H., Xu, B., Pu, J., Lu, A., Xiang, Y., Kattel, D. B., and Joswiak, D.: Different glacier status with atmospheric circulations in Tibetan Plateau and surroundings, Nat. Clim. Chang., 2, 663-667, https://doi.org/10.1038/nclimate1580, 2012.

Ye, Q., Zong, J., Tian, L., Cogley, J. G., Song, C., and Guo, W.: Glacier changes on the Tibetan Plateau derived from Landsat imagery: mid-1970s – 2000–13, J. Glaciol., 63, 273-287, https://doi.org/10.1017/jog.2016.137, 2017.

Yu, W., Nan, Z., Wang, Z., Chen, H., Wu, T., and Zhao, L.: An effective interpolation method for MODIS land surface temperature on the Qinghai-Tibet Plateau, IEEE J. Sel. Top. Appl. Earth Observ. Remote Sens., 8, 4539-4550, https://doi.org/10.1109/JSTARS.2015.2464094, 2015.

Zhang, G., Nan, Z., Hu, N., Yin, Z., Zhao, L., Cheng, G., and Mu, C.: Qinghai-Tibet Plateau permafrost at risk in the late 21st

https://doi.org/10.5194/egusphere-2026-345
Preprint. Discussion started: 4 March 2026

century, Earth Future, 10, https://doi.org/10.1029/2022EF002652, 2022.

Zhang, G., Nan, Z., Wu, X., Ji, H., and Zhao, S.: The Role of Winter Warming in Permafrost Change Over the Qinghai-Tibet Plateau, Geophys. Res. Lett., 46, 11261-11269, https://doi.org/10.1029/2019GL084292, 2019.

Zhang, G., Nan, Z., Zhao, L., Liang, Y., and Cheng, G.: Qinghai-Tibet Plateau wetting reduces permafrost thermal responses to climate warming, Earth Planet. Sci. Lett., 562, 116858, https://doi.org/10.1016/j.epsl.2021.116858, 2021.

Zhang, G., Ran, Y., Wan, W., Luo, W., Chen, W., Xu, F., and Li, X.: 100 years of lake evolution over the Qinghai–Tibet Plateau, Earth Syst. Sci. Data, 13, 3951-3966, https://doi.org/10.5194/essd-13-3951-2021, 2021.

Zhang, G., Yao, T., Xie, H., Yang, K., Zhu, L., Shum, C. K., Bolch, T., Yi, S., Allen, S., Jiang, L., Chen, W., and Ke, C.: Response of Tibetan Plateau lakes to climate change: Trends, patterns, and mechanisms, Earth-Sci. Rev., 208, 103269, https://doi.org/10.1016/j.earscirev.2020.103269, 2020.

Zhang, M., Li, R., Pei, W., Zhou, Y., Li, G., and Yang, S.: Permafrost degradation risk evaluation in the Qinghai-Tibet Plateau under climate change based on machine learning models, J. Geophys. Res.-Atmos., 129, e2023JD039611, https://doi.org/10.1029/2023JD039611, 2024.

Zhang, T., Barry, R. G., Knowles, K., Heginbottom, J. A., and Brown, J.: Statistics and characteristics of permafrost and ground-ice distribution in the Northern Hemisphere, Polar Geogr., 23, 132-154, https://doi.org/10.1080/10889379909377670, 1999.

Zhao, J., Zhao, L., Sun, Z., Hu, G., Zou, D., Xiao, M., Liu, G., Pang, Q., Du, E., Li, Z., Wu, X., Xiao, Y., Wang, L., and Zhang, W.: The thermal state of permafrost under climate change on the Qinghai-Tibet Plateau (1980-2022): a case study of the West Kunlun, The Cryosphere, 19, 4211-4236, https://doi.org/10.5194/tc-19-4211-2025, 2025.

Zhao, J., Zhao, L., Sun, Z., Niu, F., Hu, G., Zou, D., Liu, G., Du, E., Wang, C., Wang, L., Qiao, Y., Shi, J., Zhang, Y., Gao, J., Wang, Y., Li, Y., Yu, W., Zhou, H., Xing, Z., Xiao, M., Yin, L., and Wang, S.: Simulating the current and future northern limit of permafrost on the Qinghai–Tibet Plateau, The Cryosphere, 16, 4823-4846, https://doi.org/10.5194/tc-16-4823-2022, 2022.

Zhao, L., Ping, C., Yang, D., Cheng, G., Ding, Y., and Liu, S.: Changes of climate and seasonally frozen ground over the past 30 years in Qinghai–Xizang (Tibetan) Plateau, China, Glob. Planet. Change, 43, 19-31, https://doi.org/10.1016/j.gloplacha.2004.02.003, 2004.

Zhao, L., Zou, D., Hu, G., Du, E., Pang, Q., Xiao, Y., Li, R., Sheng, Y., Wu, X., and Sun, Z.: Changing climate and the permafrost environment on the Qinghai–Tibet (Xizang) plateau, Permafrost and Periglacial Processes, 31, 396-405, https://doi.org/10.1002/ppp.2056, 2020.

Zhao, L., Zou, D., Hu, G., Wu, T., Du, E., Liu, G., Xiao, Y., Li, R., Pang, Q., Qiao, Y., Wu, X., Sun, Z., Xing, Z., Sheng, Y., Zhao, Y., Shi, J., Xie, C., Wang, L., Wang, C., and Cheng, G.: A synthesis dataset of permafrost thermal state for the Qinghai–Tibet (Xizang) Plateau, China, Earth Syst. Sci. Data, 13, 4207-4218, https://doi.org/10.5194/essd-13-4207-2021, 2021.

Zhao, S. P., Nan, Z. T., Huang, Y. B., and Zhao, L.: The application and evaluation of simple permafrost distribution models

https://doi.org/10.5194/egusphere-2026-345
Preprint. Discussion started: 4 March 2026

on the Qinghai–Tibet Plateau, Permafrost and Periglacial Processes, 28, 391-404, https://doi.org/10.1002/ppp.1939, 2017.

Zhao, Y., Liao, J., Zhang, Q., Chen, J., Gong, X., Shi, Y., Shi, M., Yang, D., Fan, S., Zhou, X., Cao, L., and Hu, K.: Development of China Ground Climate Normal Value Dataset from 1991 to 2020, Chinese Journal of Atmospheric Sciences, 48, 555-571, https://doi.org/10.3878/j.issn.1006-9895.2204.22010, 2024 (in Chinese).

Zhong, L., Lei, H., and Yang, J.: Development of a distributed physics-informed deep learning hydrological model for data-scarce regions, Water Resour. Res., 60, e2023WR036333, https://doi.org/10.1029/2023WR036333, 2024.

Zhou, G., Ren, H., Zhang, L., Lv, X., and Zhou, M.: Annual vegetation maps in the Qinghai–Tibet Plateau (QTP) from 2000 to 2022 based on MODIS series satellite imagery, Earth Syst. Sci. Data, 17, 773-797, https://doi.org/10.5194/essd-17-773-2025, 2025.

Zhu, Y., Sang, Y., Chen, D., Sivakumar, B., and Li, D.: Effects of the South Asian summer monsoon anomaly on interannual variations in precipitation over the South-Central Tibetan Plateau, Environ. Res. Lett., 15, 124067, https://doi.org/10.1088/1748-9326/abc71b, 2020.

Zou, D., Zhao, L., Hu, G., Du, E., Liu, G., Wang, C., and Li, W.: Permafrost temperature baseline at 15 m depth on the Qinghai–Tibetan Plateau (2010–2019), Earth Syst. Sci. Data, 17, 1731-1742, https://doi.org/10.5194/essd-17-1731-2025, 2025.

Zou, D., Zhao, L., Sheng, Y., Chen, J., Hu, G., Wu, T., Wu, J., Xie, C., Wu, X., Pang, Q., Wang, W., Du, E., Li, W., Liu, G., Li, J., Qin, Y., Qiao, Y., Wang, Z., Shi, J., and Cheng, G.: A new map of permafrost distribution on the Tibetan Plateau, The Cryosphere, 11, 2527-2542, https://doi.org/10.5194/tc-11-2527-2017, 2017.